LIVERPOOL JOHN MOORES UNIVERSITY

LJMU Research Online

Sun, F, Egami, E, Pirzkal, N, Rieke, M, Baum, S, Boyer, M, Boyett, K, Bunker, AJ, Cameron, AJ, Curti, M, Eisenstein, DJ, Gennaro, M, Greene, TP, Jaffe, D, Kelly, D, Koekemoer, AM, Kumari, N, Maiolino, R, Maseda, M, Perna, M, Rest, A, Robertson, BE, Schlawin, E, Smit, R, Stansberry, J, Sunnquist, B, Tacchella, S, Williams, CC and Willmer, CNA

First Sample of Hα+[O iii]λ5007 Line Emitters at z > 6 Through JWST/NIRCam Slitless Spectroscopy: Physical Properties and Line-luminosity Functions

http://researchonline.ljmu.ac.uk/id/eprint/22086/

Article

Citation (please note it is advisable to refer to the publisher's version if you intend to cite from this work)

Sun, F, Egami, E, Pirzkal, N, Rieke, M, Baum, S, Boyer, M, Boyett, K, Bunker, AJ, Cameron, AJ, Curti, M, Eisenstein, DJ, Gennaro, M, Greene, TP, Jaffe, D, Kelly, D, Koekemoer, AM, Kumari, N, Maiolino, R, Maseda, M, Perna, M, Rest, A, Robertson, BE, Schlawin, E, Smit, R, Stansberry, J, Sunnquist, B,

LJMU has developed **LJMU Research Online** for users to access the research output of the University more effectively. Copyright © and Moral Rights for the papers on this site are retained by the individual authors and/or other copyright owners. Users may download and/or print one copy of any article(s) in LJMU Research Online to facilitate their private study or for non-commercial research. You may not engage in further distribution of the material or use it for any profit-making activities or any commercial gain.

The version presented here may differ from the published version or from the version of the record. Please see the repository URL above for details on accessing the published version and note that access may require a subscription.

http://researchonline.ljmu.ac.uk/

For more information please contact researchonline@ljmu.ac.uk

http://researchonline.ljmu.ac.uk/

The Astrophysical Journal, 953:53 (19pp), 2023 August 10 https://doi.org/10.3847/1538-4357/acd53c
© 2023. The Author(s). Published by the American Astronomical Society.
OPEN ACCESS

First Sample of Hα+[O III]λ5007 Line Emitters at $z > 6$ Through JWST/NIRCam Slitless Spectroscopy: Physical Properties and Line-luminosity Functions

Fengwu Sun[1], Eiichi Egami[1], Nor Pirzkal[2], Marcia Rieke[1], Stefi Baum[3], Martha Boyer[4], Kristan Boyett[5,6], Andrew J. Bunker[7], Alex J. Cameron[8], Mirko Curti[9,10], Daniel J. Eisenstein[11], Mario Gennaro[4,12], Thomas P. Greene[13], Daniel Jaffe[14], Doug Kelly[1], Anton M. Koekemoer[4], Nimisha Kumari[15], Roberto Maiolino[9,10,16], Michael Maseda[17], Michele Perna[18], Armin Rest[4,12], Brant E. Robertson[19], Everett Schlawin[1], Renske Smit[20], John Stansberry[4], Ben Sunnquist[4], Sandro Tacchella[9,10], Christina C. Williams[1,21], and Christopher N. A. Willmer[1]
[1] Steward Observatory, University of Arizona, 933 North Cherry Avenue, Tucson, AZ 85721, USA; fengwusun@arizona.edu
[2] ESA/AURA STScI, 3700 San Martin Drive, Baltimore, MD 21218, USA
[3] Dept of Physics & Astronomy, University of Manitoba, Winnipeg MB R3T 2N2, Canada
[4] Space Telescope Science Institute, 3700 San Martin Drive, Baltimore, MD 21218, USA
[5] School of Physics, University of Melbourne, Parkville 3010, VIC, Australia
[6] ARC Centre of Excellence for All Sky Astrophysics in 3 Dimensions (ASTRO 3D), Australia
[7] University of Oxford, Department of Physics, Denys Wilkinson Building, Keble Road, Oxford OX13RH, UK
[8] Sub-department of Astrophysics, University of Oxford, Keble Road, Oxford OX1 3RH, UK
[9] Kavli Institute for Cosmology, University of Cambridge, Madingley Road, Cambridge CB3 0HA, UK
[10] Cavendish Laboratory—Astrophysics Group, University of Cambridge, 19 JJ Thompson Avenue, Cambridge CB3 0HE, UK
[11] Center for Astrophysics, Harvard & Smithsonian, 60 Garden Street, Cambridge, MA 02138, USA
[12] Department of Physics and Astronomy, Johns Hopkins University, 3400 North Charles Street, Baltimore, MD 21218, USA
[13] Space Science and Astrobiology Division, NASA Ames Research Center, MS 245-6, Moffett Field, CA 94035, USA
[14] Department of Astronomy, University of Texas at Austin, 2515 Speedway Boulevard Stop C1400, Austin, TX 78712, USA
[15] AURA for the European Space Agency (ESA), Space Telescope Science Institute, 3700 San Martin Drive, Baltimore, MD 21218, USA
[16] Department of Physics and Astronomy, University College London, Gower Street, London WC1E 6BT, UK
[17] Department of Astronomy, University of Wisconsin-Madison, 475 North Charter Street, Madison, WI 53706, USA
[18] Centro de Astrobiología (CAB), CSIC-INTA, Carretera de Ajalvir, Km. 4, E-28850 Torrejón de Ardoz, Madrid, Spain
[19] Department of Astronomy and Astrophysics, University of California, Santa Cruz, 1156 High Street, Santa Cruz, CA 95064, USA
[20] Astrophysics Research Institute, Liverpool John Moores University, 146 Brownlow Hill, Liverpool L3 5RF, UK
[21] NSF's National Optical-Infrared Astronomy Research Laboratory, 950 North Cherry Avenue, Tucson, AZ 85719, USA
Received 2022 September 7; revised 2023 May 10; accepted 2023 May 11; published 2023 August 1

Abstract

We present a sample of four emission-line galaxies at $z = 6.11$–6.35 that were serendipitously discovered using the commissioning data for the James Webb Space Telescope (JWST)/NIRCam wide-field slitless spectroscopy mode. One of them (at $z = 6.11$) has been reported previously, while the others are new discoveries. These sources are selected by the secure detections of both [O III] λ5007 and Hα lines with other fainter lines, which were tentatively detected in some cases (e.g., [O II] λ3727, [O III] λ4959). In the [O III]/Hβ–[N II]/Hα Baldwin–Phillips–Terlevich diagram, these galaxies occupy the same parameter space as that of $z \sim 2$ star-forming galaxies, indicating that they have been enriched rapidly to subsolar metallicities ($\sim 0.4\,Z_{\odot}$), similar to galaxies with comparable stellar masses at much lower redshifts. The detection of strong Hα lines suggests a higher ionizing photon production efficiency within galaxies in the early universe. We find brightening of the [O III] λ5007 line-luminosity function (LF) from $z = 3$ to 6, and weak or no redshift evolution of the Hα line LF from $z = 2$ to 6. Both LFs are underpredicted at $z \sim 6$ by a factor of ∼10 in certain cosmological simulations. This further indicates a global Lyα photon escape fraction of 7%–10% at $z \sim 6$, which is slightly lower than previous estimates through the comparison of the UV-derived star formation rate density and Lyα luminosity density. Our sample recovers 66^{+128}_{-44}% of $z = 6.0$–6.6 galaxies in the survey volume with stellar masses greater than $5 \times 10^8\,M_{\odot}$, suggesting the ubiquity of strong Hα and [O III] line emitters in the Epoch of Reionization, which will be further uncovered in the era of JWST.

Unified Astronomy Thesaurus concepts: Emission line galaxies (459); High-redshift galaxies (734); James Webb Space Telescope (2291); Starburst galaxies (1570); Galaxy spectroscopy (2171)

1. Introduction

With 18 images of the same star from each segment of the primary mirror finally aligned together, the long-awaited James Webb Space Telescope (JWST; Gardner et al. 2023) has immediately started to unfold the secrets from the distant universe. Thanks to its unprecedented sensitivity and spectroscopic capability in the near-/mid-infrared (NIR/MIR) wavelengths, for the first time the rest-frame optical nebular emission lines (e.g., [O II] λλ 3726, 3729, Hβ, [O III] λλ 4959, 5007 and Hα) of normal star-forming galaxies can be directly detected and resolved in the Epoch of Reionization (EoR: $z \gtrsim 6$; see a recent review by Robertson 2022). The JWST/NIRSpec Early-release Observations (EROs) of the SMACS0723 lensing-cluster field (Pontoppidan et al. 2022) have immediately produced high-quality spectra for a handful of $z \sim 8$ galaxies with low stellar masses ($M_{\rm star} \lesssim 10^8\,M_{\odot}$). This allows numerous studies, including direct gas-phase metallicity measurements (see Arellano-Córdova et al. 2022;

Original content from this work may be used under the terms of the Creative Commons Attribution 4.0 licence. Any further distribution of this work must maintain attribution to the author(s) and the title of the work, journal citation and DOI.

Brinchmann 2023; Schaerer et al. 2022; Tacchella et al. 2022; Taylor et al. 2022; Carnall et al. 2023; Curti et al. 2023; Katz et al. 2023; Rhoads et al. 2023; Trump et al. 2023). These ERO results have clearly demonstrated the power of JWST's spectroscopic observations, initially with NIRSpec, promising many exciting discoveries to be made over the coming years.

In addition to NIRSpec, NIRCam's wide-field slitless spectroscopy (WFSS; Greene et al. 2017; Rieke et al. 2023) mode offers a uniquely powerful capability, allowing us to conduct blind (i.e., unbiased) surveys of EoR galaxies with strong line emissions in the rest-frame optical. Studies in recent years have shown that there exists a substantial population of star-forming galaxies at $z \gtrsim 6$ whose rest-frame emission lines may be strong enough to distort Spitzer/IRAC [3.6]–[4.5] μm broadband colors (e.g., Egami et al. 2005; Schaerer & de Barros 2009; Labbé et al. 2013; Stark et al. 2013; Smit et al. 2014, 2015; Roberts-Borsani et al. 2016; Harikane et al. 2018; Endsley et al. 2021a, 2021b). Although NIRCam/Grism spectroscopy is not as sensitive as that of NIRSpec because of a higher background, the NIRCam WFSS mode has the potential to sample a substantial number of line-emitting galaxies in the EoR. Indeed, this has become a real possibility with the serendipitous discovery of a line emitter at $z = 6.11$ with bright [O III] λ5007 and Hα emission lines in the shallow ($\sim$20 minutes integration) NIRCam WFSS commissioning data (Sun et al. 2022b; hereafter Paper I), which confirms the ubiquity of galaxies with strong rest-frame optical emission in the EoR.

Scientifically, a unique power of NIRCam WFSS data is its ability to directly measure or constrain the luminosity functions (LFs) of strong rest-frame optical lines at $z \gtrsim 6$. However, this will be difficult with NIRSpec multi-object spectroscopy (MOS) observations because of (i) complex target selection functions that are inherent in various criteria based on continuum colors and (ii) wavelength-dependent slit losses. This is also impossible with NIRISS WFSS observations because of a shorter wavelength coverage (0.8–2.2 μm, in contrast to 2.4–5.0 μm of NIRCam WFSS). The emergence of strong line emitters inferred from the IRAC observations mentioned above suggests a significant brightening of the corresponding line LF toward high redshift. Indeed, a recent estimate of the $z \sim 8$ [O III]+Hβ LF by De Barros et al. (2019) shows such a trend. This is in great contrast to the rapid dimming seen with the Lyα LF (e.g., Konno et al. 2018) and that of UV continuum (e.g., Bouwens et al. 2016a, 2021). While the former reflects absorption because of increasingly neutral IGM at high redshift, the combination of increasing [O III]+Hβ and decreasing UV luminosities would imply a systematic increase of the hydrogen ionizing production efficiency ($\xi_{\rm ion}$) in these galaxies (i.e., more hydrogen atoms are ionized for a given UV luminosity), which has been directly observed in strong [O III] emitters at $z = 1.3 - 2.4$ (e.g., Tang et al. 2019). NIRCam WFSS surveys targeting EoR galaxies will enable accurate and robust determination of line LFs in the rest-frame optical, which will allow us to investigate these issues directly.

In this work, we present a sample of four [O III] λ5007 and Hα line emitters at $z > 6$ that were discovered serendipitously with the JWST/NIRCam WFSS mode. These galaxies were discovered in the field around the flux-calibration star P330-E (GSC 02581-02323), which was observed during the commissioning phase of this observing mode. Among them, the lowest-redshift source at $z = 6.11$ has been reported in Paper I, and the other three sources at $z = 6.15$–6.35 are reported for the first time. The detections of both [O III] and Hα emission lines for all sources provide secure spectroscopic redshift determination, and also enable the determination of their physical properties and emission-line LF.

This paper is arranged as follows. In Section 2, we describe the JWST/NIRCam observations and corresponding data reduction techniques. The spectroscopic and photometric measurements are presented in Section 3. In Section 4, we discuss the physical properties of these emission-line galaxies, including the line strengths, metallicities, ionizing photon production efficiency, and the [O III]/Hβ–[N II]/Hα Baldwin–Phillips–Terlevich (BPT; Baldwin et al. 1981) diagram of galaxies at $z > 6$. In Section 5, we discuss the volume density of these galaxies in the EoR, presenting the first direct measurements of the [O III] λ5007 and Hα line LFs at $z > 6$. The conclusions can be found in Section 6. Throughout this paper, we assume a flat ΛCDM cosmology with $H_0 = 70$ km s^{-1} Mpc^{-1} and $\Omega_m = 0.3$, and a Chabrier (2003) initial mass function (IMF). The AB magnitude system (Oke & Gunn 1983) is used.

2. Observation and Data Reduction

The JWST/NIRCam long-wavelength (LW; 2.4–5.0 μm) grism characterization observations were conducted through Program #1076 (PI: Pirzkal) during the commissioning phase of the instrument (Rieke et al. 2023; Rigby et al. 2023). Both grism spectroscopic and direct-imaging observations were performed with the flux-calibration star P330-E (a solar analog) and the wavelength-calibration star IRAS 05248-7007 (a post-Asymptotic-Giant-Branch star in the Large Magellanic Cloud). The obtained data were also described in Paper I.

2.1. Direct Imaging

The imaging data of the P330-E field were taken either simultaneously with the grism exposures (short-wavelength, SW filter: F212N) or after the grism observations through direct and out-of-field imaging (SW filter: F212N; LW filter: F250M, F322W2, F335M, and F444W). Among them, the shallow F250M and F335M data were taken with the observations #103/104 as part of the early spectral calibration on UT 2022 April 5. The total integration times were 6.4 and 4.3 minutes (three integrations each), respectively. The F322W2 and F444W imaging data were taken through the observations #105-108 and #109-112, respectively. The total integration time was 4 minutes (11 integrations each) with either of the two filters.

For the shallow F212N data, we only used 31 integrations associated with the LW grism exposures because the integrations were longer (96 s each). Shorter F212N integrations (21 s each, 8 minutes in total) taken with out-of-field imaging were not included because they caused problems for the TWEAKREG step in JWST[22] Stage-3 mosaicking pipeline in source identification and world-coordinate-system (WCS) registration. The final mosaicked F212N image has a total integration time of 50 minutes.

The direct-imaging data were reduced and mosaicked using a modified Stage-1/2/3 JWST pipeline 1.8.2 and CRDS

[22] https://github.com/spacetelescope/jwst

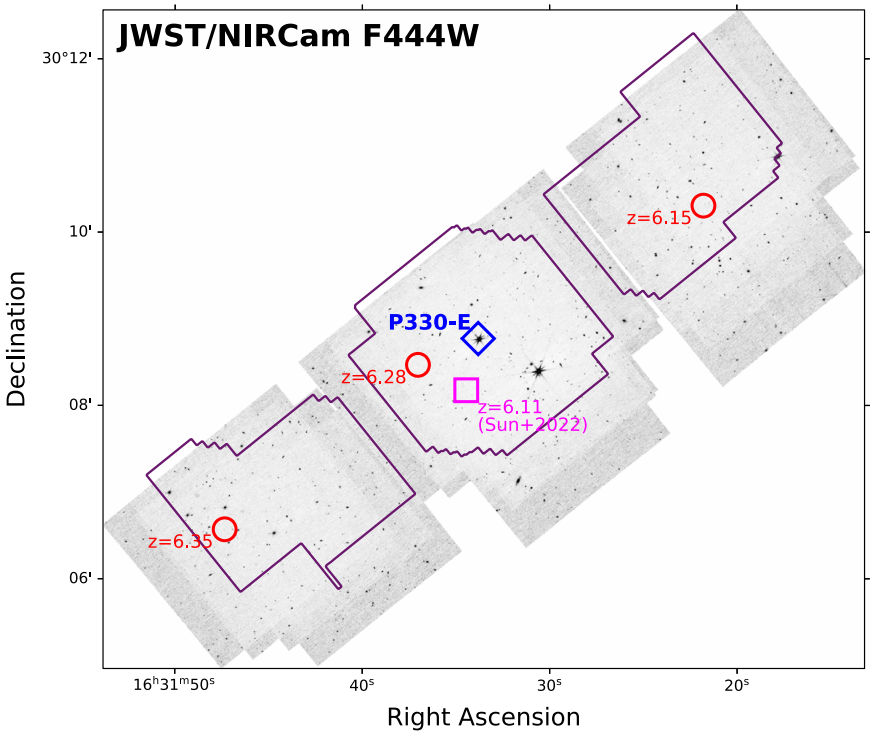

Figure 1. JWST/NIRCam F444W map of the P330-E field. The open-blue diamond denotes the primary target (P330-E as the flux calibrator) of the obtained observations. The $z = 6.11$ [O III] and Hα line emitter discovered by Sun et al. (2022a, Paper I) is shown in the open magenta square, and the three newly discovered [O III] and Hα line emitters (this work, $z = 6.15 - 6.35$) are shown in open red circles. The purple contours denote the regions in which sources can potentially yield both [O III] and Hα line detections with this survey at $z = 6.2$ (see Appendix).

calibration reference file context `jwst_1041.pmap`. This version has included the Cycle-1 NIRCam photometric zero-points (see Boyer et al. 2022 and Rigby et al. 2023). The so-called $1/f$ noise (see Schlawin et al. 2020) was modeled and removed using the code TSHIRT/ROEBA[23] for stage-2 products (i.e., the `_cal.fits` files). The snowball artifacts from cosmic rays were identified and masked through their large-area jump-detection information ($\geqslant$60 native pixels) on the data-quality map of each individual integration. The final image products were resampled to a native pixel size of $0\farcs0312$ (SW) and $0\farcs0629$ (LW) with `pixfrac` $= 0.8$, and the WCS of the images were registered with the GAIA DR2 catalog (Gaia Collaboration et al. 2018). More specifically, we registered the F444W mosaic image to the GAIA catalog, and then registered the images in all of the other filters to the frame of the F444W image. The mosaicked F444W image of the P330-E field is displayed in Figure 1.

Finally, we performed source extraction with the mosaicked F322W2 and F444W images using SEXTRACTOR v2.25.3 (Bertin & Arnouts 1996) in the single-image detection mode down to 5σ detection levels. The depths are $\sim$25.5 and 24.9 AB mag in the F322W2 and F444W band, respectively, which are derived using the automatic Kron aperture and sky background measured from local annulus.

2.2. Grism Spectroscopy

As described in Paper I, the WFSS observations of the P330-E field were obtained with both the F322W2 (2.4–4.0 μm) and F444W (3.9–5.0 μm) filters on UT 2022 April 29. The spectral resolution is $R \sim 1600$ at around 4 μm, and the dispersion is $\sim$1 nm pixel^{-1}. In each band, the target was observed with four module (A/B)/grism (R/C; orthogonal) combinations (AR, AC, BR, and BC) at four INTRAMODULEX primary dither positions, respectively. With the five-group BRIGHT1 readout pattern, the effective exposure time per integration was 96 s. Following Paper I, the last integration with the Module B Grism C in the F322W2 band (Observation #108, Visit 001, Exposure 4) was not used in our analysis because of unstable guiding. The maximum exposure time for a source is $\sim$25 minutes in each band after combining integrations with all grisms. However, we also note that the actual effective exposure time could be shorter, depending on the wavelength of interest and the sky position of the source. Therefore, the median exposure time in each band is $\sim$10 minutes. We refer the reader to the JWST User Documentation[24] and Rieke et al. (2023) for further information.

The WFSS data were reduced to the level of Stage-1 (i.e., _RATE files) with the same standard JWST calibration pipeline. We applied a pixel-to-pixel flat-field correction using the imaging flat data obtained with the same filter and module. This is the same method that we adopted for the F322W2/F444W grism flux calibration during the commissioning of the NIRCam/WFSS mode (also Paper I) because the large-scale grism flat-field calibration has not been complete at the time of writing. In the standard JWST pipeline, the grism background subtraction step is performed by scaling the theoretical background to that observed in each individual integration. However, the accuracy of the current theoretical background is limited by the accuracy of the sky-background spectrum and the grism tracing/dispersion model (first and second order),

[23] https://github.com/eas342/tshirt

[24] https://jwst-docs.stsci.edu/jwst-near-infrared-camera/nircam-performance/nircam-wfss-field-of-view

neither of which have yet been fully characterized. As in Paper I, we performed the 2D sky-background subtraction using the sigma-clipped median grism images.

Because the dithering of the telescope could introduce astrometric errors (i.e., the dithers might not exactly equal the commanded values), the WCS of each grism image was calibrated with the GAIA DR2 catalog by matching with the stars detected in the NIRCam SW images, which were taken simultaneously in the F212N band. We note that such a registration relies on the internal alignment between NIRCam SW and LW instrument aperture, and may introduce astrometric residuals. However, these residuals should be stable and have been included in the grism spectral tracing models.

The grism spectral tracing models, which give the relation between the spectral pixels (x_s, y_s) and the direct-imaging position (x_0, y_0), were constructed using the spectral traces of point sources observed within the P330-E field. The spectral tracing functions (e.g., $y_s(x_0, y_0, x_s)$ in Grism R) were constructed separately for the AR, AC, BR, and BC module/grism combinations in the F322W2 and F444W filters. These functions include a third-degree polynomial of x_0, y_0 and a second-degree polynomial of x_s to fit the strong curvature and field dependence of the spectral traces. With any given spectral pixel position in the dispersion direction (e.g., x_s in Grism R), our spectral tracing model can predict the position along the perpendicular direction (e.g., y_s in Grism R) with a root-mean-square (rms) accuracy of 0.1–0.2 pixel, i.e., 10%–20% of the rms width of the point-source spectral trace.

The grism dispersion models, which give the relation between the spectral pixels along the dispersion direction (e.g., x_s in Grism R) and (x_0, y_0), and wavelength of interest (λ), were constructed using the emission-line spectra of IRAS 05248–7007. Up to 11 hydrogen recombination lines in Brackett ($n = 4$), Pfund ($n = 5$) and Humphreys ($n = 6$) series were used for wavelength calibration in the F322W2 band, and up to eight lines were used in the F444W band, including hydrogen recombination lines and a He I line at 4.296 μm (rest frame). The dispersion functions (e.g., $x_s(x_0, y_0, \lambda)$ in Grism R) were simultaneously constructed separately for the AR, AC, BR, and BC module/grism combinations using the F322W2 and F444W data. These functions include a second-degree polynomial of x_0, y_0 and a third-degree polynomial of λ to perform wavelength calibration with field dependence. Our dispersion model can predict the position of a spectral feature at a wavelength of λ_s along the dispersion direction (e.g., x_s in Grism R) with an rms accuracy of 0.2 pixel, i.e., ~10% of the two-pixel resolution element.

We also used the spectra of P330-E to construct the flux-calibration functions in the F322W2 and F444W filters. Using the grism tracing and dispersion models described above, we extracted the spectra of the standard star using box apertures with a height of $D = 20$ pixels ($1\farcs26$). The corresponding aperture loss was found to be small (2%–3%) when compared with the extracted spectra with a larger aperture ($D = 100$ pixels). This loss was corrected in the following analyses. The flux-calibration functions, i.e., conversion factors from count rate (unit: DN/s) to flux density (unit: mJy) as functions of wavelength, were constructed using all of the available integrations for four grisms taken in the F322W2 and F444W filters, respectively, with a wavelength step of 0.005 μm (~5 pixels). Through the comparisons of extracted P330-E spectra in different exposures and different locations on the detector, we find that the variations of count rates are only 1%–2% when the spectra are binned to 0.005 μm. We therefore conclude that the accuracy of flux calibration is dominated by the systematic uncertainty (~2% from standard star; Gordon et al. 2022) and flat-field error (~3% for pixel variation).

The grism spectral tracing, dispersion, and flux-calibration models derived from the commissioning data have been made available online.[25] With the derived source catalog in Section 2.1 and models described above, we conducted 2D spectral extraction, wavelength, and flux calibration on the flat-fielded WFSS data, and combined the extracted 2D spectra taken with Grism R, C, and both. These were performed for ~3000 sources detected in the F322W2 and F444W images, as described in Paper I.

3. Results

3.1. Discoveries of Hα+[O III] Emitters at z > 6

We limited the search for line emitters at $z > 6$ to a survey area that could yield detections of both [O III] λ5007 (in the F322W2 band, observed wavelength $\lambda_{obs} > 3.5$ μm) and Hα lines (in the F444W band, observed wavelength $\lambda_{obs} > 4.6$ μm). These two emission lines are expected to be the most luminous lines of star-forming galaxies in the rest-frame optical and the detection of these two lines can securely determine the redshift. The effective survey area, up to 14.4 arcmin^2, depends on the redshift and expected line luminosities, which will be discussed further in the Appendix.

Line emitters were identified through visual inspection of 2D grism spectral images, 1D spectra, and 2D direct images taken in both the F322W2 and F444W bands. Because the underlying stellar continuum emission of EoR galaxies is not expected to be detectable with the shallow grism data in the combined 2D spectral images, we subtracted the median-filtered 2D background. The 1D spectra were then optimally extracted (Horne 1986) based on the Gaussian models of emission-line profiles in the spatial direction. The 1D uncertainty spectra were generated using the error extension of the 2D spectra, and we confirm that they are consistent with the rms of 1D scientific spectra. All of the line profiles in collapsed 1D spectra were modeled with Gaussian profiles, and potential [O III] and Hα emission lines with a signal-to-noise ratio (S/N) that was less than 3 were discarded from further analysis.

Among ~3000 direct-imaging sources detected in either the F322W2 or F444W bands, ~10% of them yielded potential emission-line detections (see the $z = 4.4$ [O III] and Hα line emitter in the JWST commissioning report; Rigby et al. 2023). Four sources were confirmed at $z > 6$ after careful inspection, including the $z = 6.112$ source reported in Paper I and three new sources at $z = 6.146$, 6.279 and 6.348. All of these sources yielded secure [O III] λ5007 ($>5\sigma$) and Hα ($>3\sigma$) line detections in the coadded spectra, which could be detected in both the R and C grism data separately as long as the lines are within the wavelength coverage. These galaxies are referred to as P330E-z6.11, P330E-z6.15, P330E-z6.28, and P330E-z6.35 hereafter based on the ID of the primary target in the field and their redshifts.

Figure 1 shows the locations of these $z > 6$ emission-line galaxies in the mosaicked NIRCam F444W map. The cutout

[25] https://github.com/npirzkal/GRISM_NIRCAM/

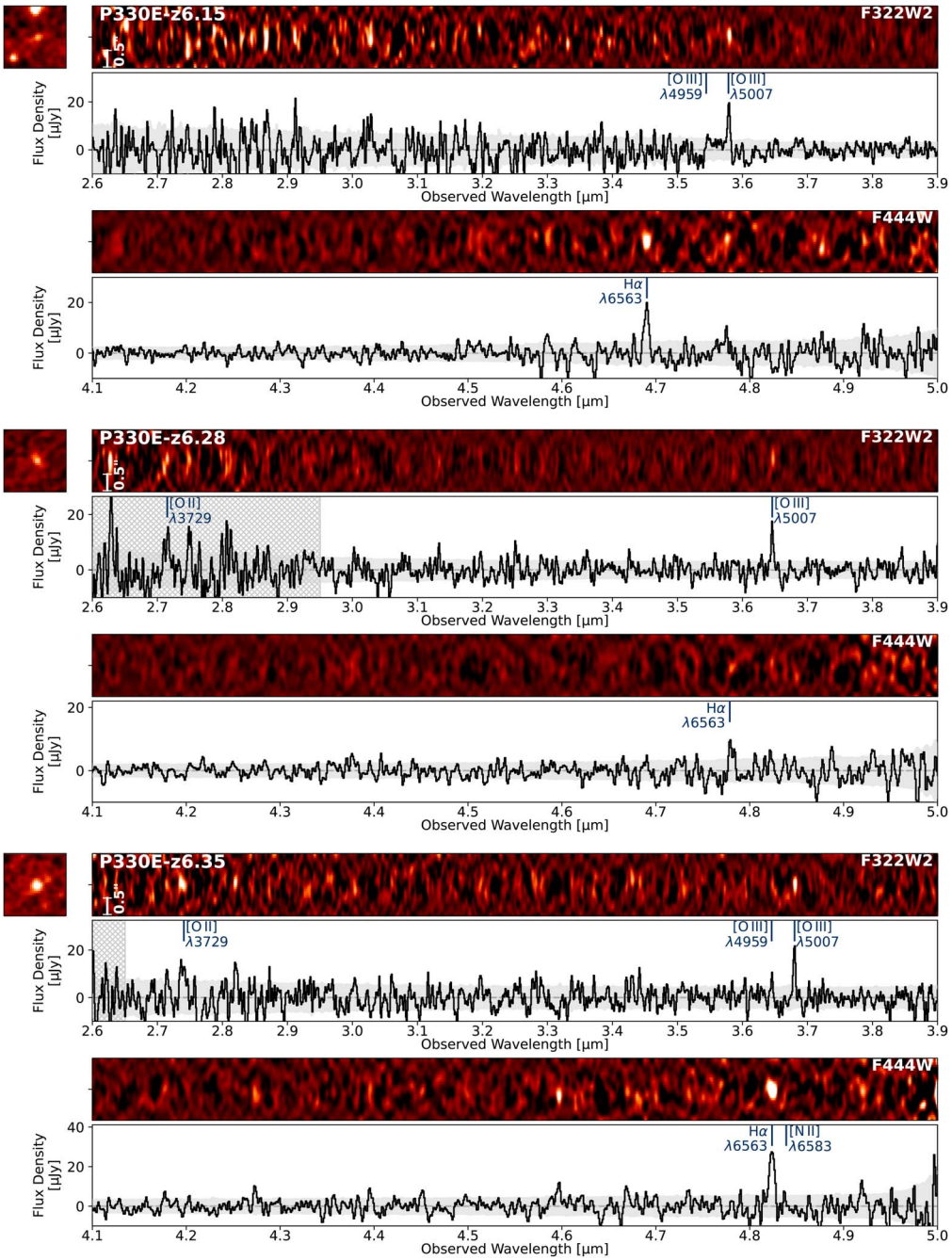

Figure 2. Discovery image and 2D/1D spectra of three [O III] and Hα line emitters at $z = 6.15$ (top), 6.28 (center) and 6.35 (bottom). In each plot, the NIRCam/F444W cutout image (size: $1\farcs9 \times 1\farcs9$) is shown in the top left-hand panel. Coadded, calibrated, and background-subtracted 2D and 1D spectra in the F322W2 and F444W band are shown on the right-hand side. Notable emission lines are labeled with dark-blue lines. The 1D error spectra are shown as the gray-shaded regions, and the wavelength ranges with overlapping continuum contaminants are shown as the gray-hatched regions. Note that the line widths of [O III] and Hα are consistent for each source, although they look different in the plot because of different intrinsic aspect ratios of the 2D spectra.

direct images, 2D spectra, and 1D spectra are shown in Figure 2 with notable emission lines labeled. Among them, P330E-z6.11 and z6.28 were always observed with the flux calibrator in the same module of NIRCam, and therefore their effective integration time is ∼20 minutes with each filter, which is roughly twice that of the other two sources. We also note that a few other suspicious lines can be identified in the 2D spectra, but most of them were only detected in the spectra produced by either the R or C grism, and therefore their associations with the sources are doubtful.

We modeled the properties of detectable emission lines (in increasing order of wavelength: [O II] λ3727, Hβ, [O III] $\lambda\lambda$ 4959, 5007, Hα and [N II] λ6583) using Gaussian profiles. Among them, Hβ+[O III] line profiles were fitted simultaneously and the line centers were controlled by the redshift parameter. Given the low significance of the detection, the Hβ and [O III] λ4959 line FWHMs were fixed to be the same as those of the [O III] λ5007 lines. Hα+[N II] λ6583 lines were modeled in the same way. The best-fit redshift parameters are consistent with those derived from Hβ+[O III] fitting within

Table 1
Summary of the Properties of $z > 6$ Hα and [O III] Emitters in This Work

	P330E-z6.11	P330E-z6.15	P330E-z6.28	P330E-z6.35
R.A.	16:31:34.46	16:31:21.79	16:31:37.02	16:31:47.34
Decl.	+30:08:10.5	+30:10:18.4	+30:08:28.1	+30:06:34.2
Redshift	6.112 ± 0.001	6.145 ± 0.001	6.280 ± 0.001	6.348 ± 0.001
Photometric Properties				
F212N [AB mag]	>23.8	>24.1	24.74 ± 0.75	>23.5
F250M [AB mag]	25.01 ± 0.42	...	23.88 ± 0.16	...
F322W2 [AB mag]	24.27 ± 0.09	25.60 ± 0.31	23.70 ± 0.05	24.31 ± 0.15
F335M [AB mag]	25.15 ± 0.36	...	24.45 ± 0.20	...
F444W [AB mag]	24.18 ± 0.15	25.17 ± 0.32	23.89 ± 0.11	23.77 ± 0.12
Spectroscopic Properties				
f([O II] λ3727) [10^{-18} erg s^{-1} cm^{-2}]	<30.9	<52.3	22.2 ± 9.5	30.7 ± 10.9
f(Hβ) [10^{-18} erg s^{-1} cm^{-2}]	7.1 ± 2.8	<15.6	<5.2	<9.6
f([O III] λ4959) [10^{-18} erg s^{-1} cm^{-2}]	9.9 ± 2.7	7.3 ± 3.6	2.1 ± 1.7	8.7 ± 3.1
f([O III] λ5007) [10^{-18} erg s^{-1} cm^{-2}]	34.8 ± 3.2	24.8 ± 4.1	13.8 ± 2.1	20.9 ± 3.6
f(Hα)[10^{-18} erg s^{-1} cm^{-2}]	14.7 ± 2.6	16.9 ± 3.2	7.6 ± 2.3	26.5 ± 3.8
f([N II] λ6583) [10^{-18} erg s^{-1} cm^{-2}]	<6.3	<7.0	<5.8	3.6 ± 2.9
EW([O II] λ3727) [Å]	<213	...	97 ± 45	291 ± 114
EW(Hβ) [Å]	70 ± 29	<729	<35	<94
EW([O III] λ4959) [Å]	100 ± 30	344 ± 254	14 ± 12	85 ± 33
EW([O III] λ5007) [Å]	359 ± 60	1165 ± 670	97 ± 22	205 ± 49
EW(Hα) [Å]	221 ± 50	841 ± 489	84 ± 29	267 ± 59
EW([N II] λ6583) [Å]	<96	<353	<63	36 ± 30
Physical Properties				
log[$M_{\rm star}/M_\odot$]	9.1 ± 0.2	8.9 ± 0.4	9.2 ± 0.3	9.5 ± 0.3
SFR(Hα) [$M_\odot$ yr^{-1}]	32 ± 5	38 ± 7	18 ± 5	64 ± 9
SFR(SED,UV) [$M_\odot$ yr^{-1}]	25 ± 7	7 ± 4	60 ± 17	22 ± 10
log[$\xi_{\rm ion}$/(erg^{-1} Hz)]	25.2 ± 0.1	25.8 ± 0.3	24.6 ± 0.2	25.5 ± 0.2
12 + log(O/H)	8.2 ± 0.2	8.3 ± 0.2	8.2 ± 0.3	8.4 ± 0.2

Note. Properties of P330E-z6.11 were reported in Sun et al. (2022b), but here we update all measurements with the latest flux calibration.

$\Delta z \sim 0.001$, which demonstrates the accuracy of the wavelength calibration. We fitted the flux of the [O II] $\lambda\lambda$ 3726, 3729 lines using a single Gaussian profile at λ3727 because the doublet cannot be resolved. In this fit, the redshift parameter was fixed and the line FWHM was set to be identical to the average FWHM of the Hα and [O III] lines to mitigate the artificial broadening and flux-boosting effect because of low significance of the line detections (see discussion in Appendix).

All of the line flux measurements are presented in Table 1. In addition to the firm detections of [O III] λ5007 and Hα lines, [O II] λ3727 lines were detected in P330E-z6.28/z6.35 at $\sim 2.6\sigma$, which appear to be more luminous than their [O III] λ5007 lines. Hβ was not detected for the three new sources presented here, while the 3σ upper limits of line fluxes are consistent with or higher than those estimated from Hα line fluxes assuming Case B recombination with a typical electron temperature of $T_e = 10^4$ K (Hα/Hβ = 2.86; Osterbrock & Ferland 2006). The [O III] λ4959 lines were also tentatively detected for all sources (up to 3.7σ) and the line ratios to [O III] λ5007 line are consistent with the theoretical ratio of 1/3. Finally, the significance of [N II] λ6583 line is $<2\sigma$ for all sources in our sample.

3.2. Photometry and Line Equivalent Widths

Similar to Paper I, we performed aperture photometry of all $z > 6$ line-emitting galaxies in F212N, F250M, F322W2, F335M, and F444W bands. Unlike P330E-z6.11, which has a clear two-component structure, the three new sources found in this work were detected as single-component systems and their angular sizes are generally compact (FWHM $\lesssim 0\farcs25$). We adopted a conservative circular aperture of $r = 0\farcs45$ using PHOTUTILS (Bradley et al. 2020) to avoid missing extended components and minimize the aperture loss, similar to that used in Paper I. With such an aperture radius, the variation of the encircled light fractions of point spread functions at 2–5 μm is $\sim$3%, which is much smaller than the photometric uncertainty. We also modeled the F444W surface brightness profiles of sources in our sample with the 2D Gaussian model, and we confirmed that the aperture loss is negligible. We subtracted the sky background using the median of sigma-clipped local annulus, and computed the photometric uncertainty using the rms of that. Broadband photometry is summarized in Table 1.

All sources were detected in the broad F322W2 and F444W bands, but remained undetected within the narrow F212N filter. For P330E-z6.28 with the F250M and F335M coverage, we were able to detect its rest-frame UV continuum (23.88 ± 0.16 AB mag in the F250M band) and optical stellar continuum (24.45 ± 0.20 AB mag in the F335M band). At this redshift, no strong emission line is expected in the wavelength range of the F250M and F335M filters, but the flux densities measured with the broad F322W2 and F444W filters could be boosted by strong [O III] and Hα lines, respectively. Indeed, we find a blue F250M–

F335M color of -0.57 ± 0.26 and an F322W2–F335M excess of 0.75 ± 0.21 mag, which both suggest the presence of strong nebular emission lines (e.g., [O III]) and potentially nebular continuum blueward of the Balmer break ($\lambda_{\rm rest} < 3640$ Å).

With the continuum photometry, we computed the line equivalent widths (EWs). To estimate the underlying continuum flux density, we subtracted all measured line fluxes within the passband for all broadband photometric measurements redward of the Balmer break (F322W2, F444W, and F335M if available). The continuum flux densities were then modeled with a power-law function $f_\nu \propto \lambda^\alpha$. We then computed the line EW using the underlying continuum strength estimated at the line wavelength. All of the line EWs are reported in Table 1. However, we also note that the broadband flux density could be slightly overestimated because of the contribution from undetected faint emission lines that may not have been properly subtracted, which could potentially lead to underestimates in line EWs. The Balmer discontinuity can also introduce errors into the continuum flux density determination in the F322W2 band.

4. Discussion I: Physical Properties

4.1. SED Modeling

To derive the physical properties of galaxies in our sample, we perform SED modeling with CIGALE (Boquien et al. 2019). Broadband photometry and the EWs of [O III] and Hα lines are included as constraints. [O II], Hβ and [N II] line EWs are not included given the general low significance of detections. Similar to Paper I, we assume a commonly used delayed star formation history (SFH; `sfhdelayed`), in which SFR(t) $\propto t \exp(-t/\tau)$ and τ is the peak time of SFH. An optional late starburst is allowed in the last 1–5 Myr, which can contribute to 0%–80% of the total stellar mass. We use Bruzual & Charlot (2003) stellar population synthesis models. We also allow a metallicity range of $0.2\,Z_\odot$ to $Z_\odot$, a broad ionization parameter ($\log U$) range of -1.0 to -3.5. We adopt the Calzetti et al. (2000) attenuation curve and the color excess of the nebular lines is allowed between $E(B-V)_{\rm line} = 0-1$.

The best-fit SED models are shown in Figure 3. The best-fit SEDs are rich in emission lines, which indicates that the galaxies are young and star-forming. However, most of the lines are too faint to be detected in the grism spectra. Similar to the results in Paper I, the best-fit SFH models typically invoke both young (1–2 Myr) and old (∼300 Myr) stellar populations. Roughly half of the stellar masses in all galaxies are produced by the most recent starburst, which is consistent with the presence of strong nebular emission lines. We note that this result is driven by the large emission-line EWs. If the fitting is performed without line EWs, then the amount of recent star formation will decrease sharply.

The median mass-weighted stellar age of sources in our sample is 74 ± 50 Myr and the median stellar mass ($M_{\rm star}$) is $1.4^{+0.7}_{-0.5} \times 10^9\,M_\odot$. Dust attenuation is negligible for P330E-z6.11/6.28, which is likely not the case for P330E-z6.15 ($A_V = 1.1 \pm 0.7$ for stellar continuum) and P330E-z6.35 ($A_V = 1.4 \pm 0.7$) as indicated by their red F322W2–F444W colors, even after the subtraction of [O III] and Hα lines. However, we also note that the constraints on the dust attenuation and stellar masses are not tight given that three of the sources were only detected in the two broad LW bands.

The derived physical properties of galaxies in our sample are also presented in Table 1. The physical properties of P330E-z6.11 have been reported in Paper I, and we have updated our results with the latest flux calibration. The differences from those in Paper I are small, within 1σ significance level. Following Paper I, we also infer UV SFRs for galaxies in our sample from the best-fit SED, and the median is $24 \pm 11\,M_\odot\,{\rm yr}^{-1}$. This is smaller than the median of Hα-based SFR ($35 \pm 9\,M_\odot\,{\rm yr}^{-1}$) assuming the conversion in Kennicutt & Evans (2012, uncorrected for dust attenuation). This comparison likely indicates: (i) a bursting nature because Hα is more sensitive to the most recent star formation than UV continuum (see Kennicutt & Evans 2012); (ii) a higher ionizing photon production efficiency ($\xi_{\rm ion}$), lower metallicity, and thus smaller Hα/SFR conversion factor (e.g., Charlot et al. 2002; Brinchmann et al. 2004) at high redshift when compared with the local universe; and (iii) a higher dust extinction in the rest-frame UV than with the Hα line (see further discussions in Section 4.5).

4.2. Comparison of Line EWs with z ≃ 5–7 Galaxies

Before the launch of the JWST, the EWs of strong [O III] and Hα emission lines at high redshifts were modeled from Spitzer/IRAC photometry. In this section, we compare the line EWs of galaxies in our sample, derived from rest-frame optical spectroscopy, with those inferred previously from the IRAC SED analyses.

In the left-hand panel of Figure 4, we compare the [O III]+Hβ line EWs and stellar masses with those of $z \sim 6.8$ galaxies in Endsley et al. (2021a, 2021b). The median [O III]+Hβ line EW of the sources in our sample is 416 ± 66 Å, with the maximum and minimum of 1510 ± 757 Å (P330E-z6.15) and 122 ± 28 Å (P330E-z6.28), respectively. Before the launch of JWST, [O III]+Hβ line EWs at $z \gtrsim 4$ could only be inferred from Spitzer/IRAC SED analysis in certain redshift windows, such as $z \simeq 6.7-7.0$ (e.g., Smit et al. 2014, 2015; Endsley et al. 2021a, 2021b). Endsley et al. (2021b) reported a median [O III]+Hβ EW of 759^{+112}_{-113} Å for a sample of UV-bright ($M_{\rm UV} \lesssim -21$) galaxies at $z \sim 6.8$, and the scatter is ∼0.25 dex.

Through a Kolmogorov–Smirnov test, we confirm that the [O III]+Hβ line EW distribution of the sources in our sample is consistent with that in Endsley et al. (2021a, 2021b) over a similar stellar-mass (∼$10^9\,M_\odot$) and SFR ($\gtrsim 10\,M_\odot\,{\rm yr}^{-1}$) range. Similar to the findings in Paper I, this confirms the presence of strong rest-frame optical nebular emission lines in EoR galaxies with a wide range of line EWs (∼1 dex span). Such a wide span is also seen with certain simulations (e.g., Ceverino et al. 2021).

We derive a median Hα EW of 239 ± 45 Å for the galaxies in our sample, with a maximum and minimum of 814 ± 489 Å (P330E-z6.15) and 84 ± 29 Å (P330E-z6.28), respectively. We also compare the Hα EWs with those of $z \simeq 5.1-5.4$ galaxies reported in Rasappu et al. (2016), whose line EWs were inferred from Spitzer/IRAC SEDs. In this redshift window, the Hα lines enter the passband of IRAC Channel 2 (CH2; 4.5 μm), while Channel 1 (CH1, 3.6 μm) is free from strong emission lines, including Hβ and [O III] ($\lambda < 3.2$ μm). Therefore, a red [3.6]–[4.5] color can be used to infer the strength of Hα emission. We assumed that ∼80% of the combined Hα+[N II]+[S II] EWs reported in Rasappu et al. (2016) is from Hα, similar to the fraction assumed in their work (84%; from Anders et al. 2003).

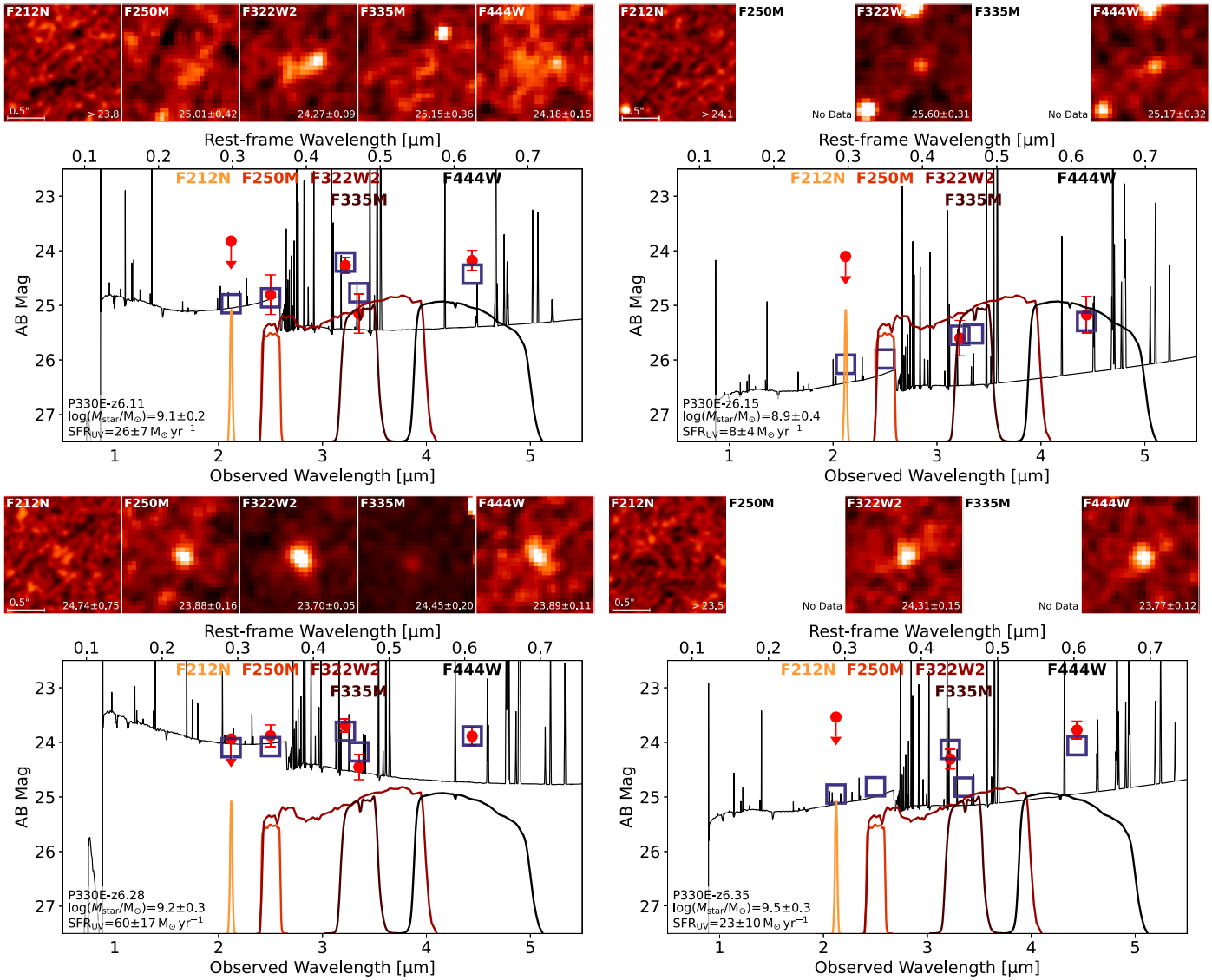

Figure 3. JWST/NIRCam multiple-wavelength cutout images and SED models of the four sources presented in this work. In each panel, we show F212N, F250M, F322W2, F335M, and F444W cutout images on the top. Measured source brightnesses are shown in the lower right-hand corner of each cutout image (unit: AB mag; 3σ upper limit for non-detection). These measurements are shown as filled-red circles in the SED plot. Best-fit SED models obtained with CIGALE are shown as black curves and best-fit source brightnesses in all filters are shown as open-blue squares. The transmission curves of all of the used filters are also shown for comparison. Derived stellar mass and UV-based SFR are shown in the lower left-hand corner of each SED plot.

With comparable stellar masses and SFRs, the median Hα EW of the galaxies with spectroscopic redshifts in Rasappu et al. (2016) is 564 ± 59 Å, 2.4 ± 0.5 times that for our sample. Although this can be potentially explained by the limited understanding of dust extinction and underlying stellar continuum in early Spitzer/IRAC studies, we cannot draw any firm conclusion from the Hα EW comparison given the small sample size.

Finally, we also compare the line EWs with those of galaxies in the local universe with comparable stellar masses. We select galaxies at $z < 0.05$ from the MPA-JHU value-added catalog of SDSS Data Release 7 (Kauffmann et al. 2003b; Abazajian et al. 2009) for comparison (black dots in Figure 4). The EWs of Hα and [O III] lines of galaxies in our sample are higher than the median EWs of SDSS-selected galaxies by at least an order of magnitude. Our conclusion remains valid if we compared with galaxies in the Portsmouth SDSS catalog (Maraston et al. 2013; Thomas et al. 2013).

4.3. Line Ratios and BPT Diagram

Despite secure identification of [O III] and Hα lines, the sources in our sample are typically undetected in either [N II] λ6583 or Hβ lines. With the latest calibrated spectra, the Hβ line of P330E-z6.11 is detected at 2.5σ, suggesting a line ratio of [O III]/H$\beta = 4.9 \pm 1.3$. None of the sources are detected in [N II] λ6583 at above 2σ, and thus the typical 3σ upper limit of [N II]/Hα line ratio is <0.4.

With these line ratios and upper/lower limits, we plot our sources on the [O III]/Hβ–[N II]/Hα BPT diagram (Baldwin et al. 1981) in Figure 5. We compare our sample with galaxies in the local universe (in the MPA-JHU catalog for SDSS Data Release 7; Abazajian et al. 2009) and $z \sim 2.3$ galaxies in the MOSDEF sample (Kriek et al. 2015; Reddy et al. 2015; Shapley et al. 2015). Although the detection rate of Hβ and [N II] lines is low, the $z > 6$ emission-line galaxies in our sample appear to occupy the same parameter space as that of

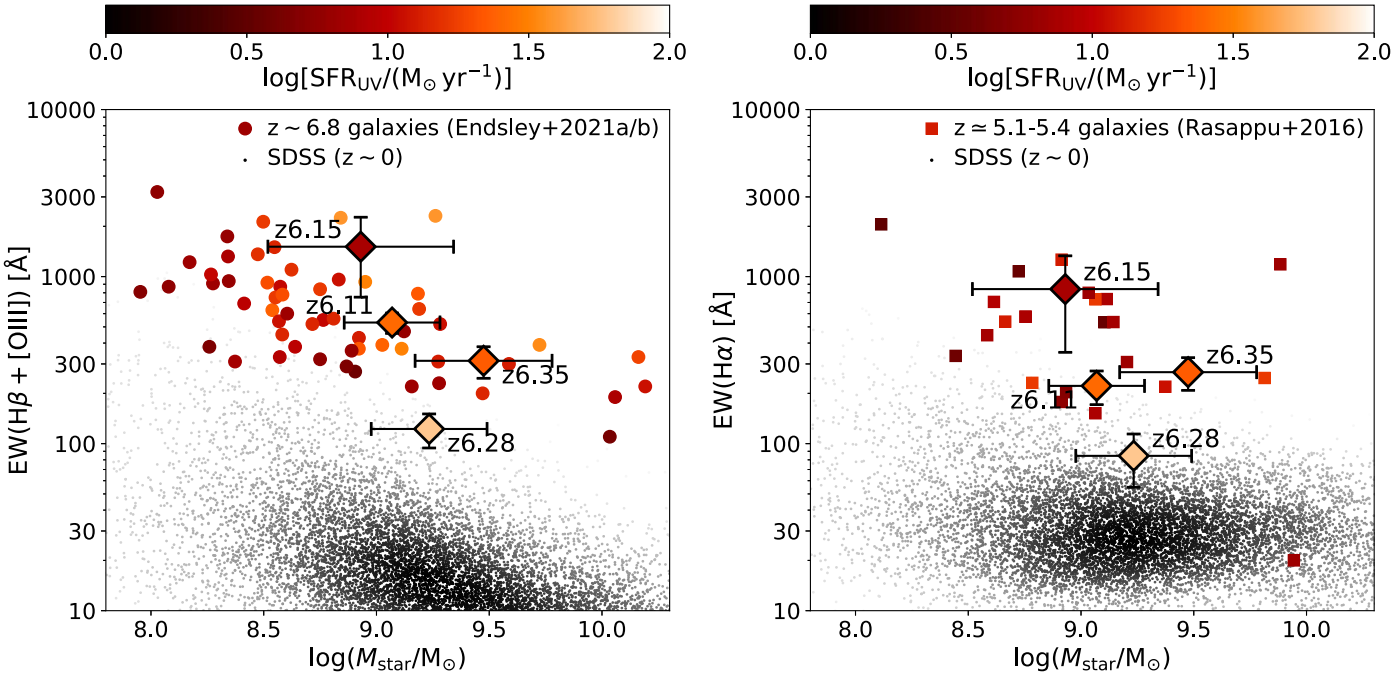

Figure 4. Left-hand panel: Hβ+[O III] EWs vs. stellar masses of sources in our sample (diamonds), compared with galaxies at $z \sim 6.8$ whose line EWs are inferred from Spitzer/IRAC [3.6]–[4.5] μm colors (circles; Endsley et al. 2021a, 2021b). Right-hand panel: Hα EWs vs. stellar masses of sources in our sample (diamonds), compared with galaxies at $z \simeq 5.1$–5.4 whose line EWs are also inferred from IRAC colors (squares; Rasappu et al. 2016). In both panels, all high-redshift sources are color-coded by their UV-based SFRs. SDSS-selected galaxies in the local universe are also shown as dots for comparison.

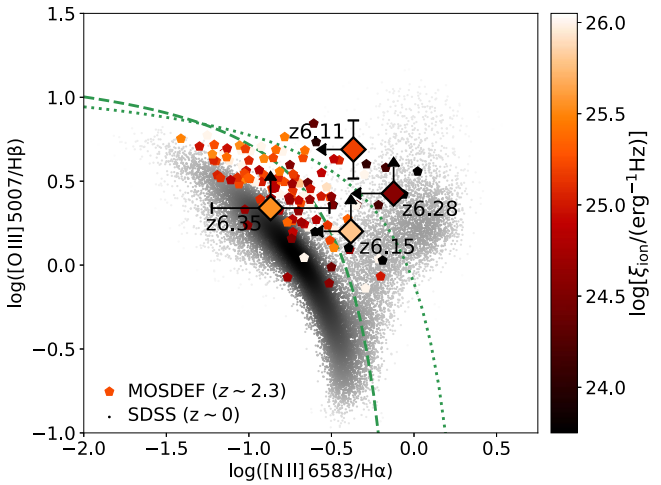

Figure 5. [O III]/Hβ–[N II]/Hα BPT diagram of $z > 6$ galaxies in our sample (diamonds), compared with those of $z \sim 2.3$ emission-line galaxies in MOSDEF sample (pentagons; Kriek et al. 2015; Reddy et al. 2015; Shapley et al. 2015). Galaxies in both samples are color-coded by their ionizing photon production efficiencies, and likely occupy the same parameter space. SDSS-selected galaxies and AGN in the local universe are shown as dots in the background, color-coded by their number densities in the parameter space. The dotted-green line is the so-called "maximum-starburst" line in Kewley et al. (2001), and the dashed-green line is the canonical AGN/star-forming galaxy boundary in Kauffmann et al. (2003a).

$z \sim 2$ star-forming galaxies in the MOSDEF sample, and are likely located above the star-forming sequence of SDSS galaxies (see also recent studies with NIRSpec, e.g., Cameron et al. 2023 and Sanders et al. 2023a). Similar to $z \sim 2$ galaxies, this could be explained by an elevated N/O abundance at a given O/H ratio and/or a higher ionization parameter (e.g., Kewley et al. 2013; Masters et al. 2014; Steidel et al. 2014; Shapley et al. 2015; Kojima et al. 2017; Curti et al. 2022) for high-redshift galaxies with moderate stellar masses ($<10^{10}$ $M_\odot$). Stars that are enhanced in alpha elements can have harder intrinsic ionization spectra, which can lead to a higher [O III]/Hβ at fixed [N II]/Hα in nebulae (e.g., Strom et al. 2017; Topping et al. 2020a, 2020b).

It is possible that sources in our sample may contain active galactic nuclei (AGNs). However, based on their locations on the BPT diagram (Kewley et al. 2001; Kauffmann et al. 2003a), hydrogen line profiles, and number density (Section 5), we do not find strong evidence to confirm any source as AGN.

4.4. Gas-phase Metallicity

With oxygen and hydrogen lines detected for all sources in our sample, we study their gas-phase metallicity using the strong-line calibrations of Bian et al. (2018). In particular, Bian et al. (2018) studied the stacked spectra of local analogs of $z \sim 2$ star-forming galaxies, derived direct gas-phase O/H abundances using [O III] λ4363 lines, and established empirical metallicity calibrations between O/H abundances and strong-line ratios, such as [N II] λ6583/Hα (also known as N2), [O III] λ5007/Hβ, ([O III] $\lambda\lambda$ 4959,5007+[O II] λ3727)/Hβ (also known as R23) and [O III] $\lambda\lambda$ 4959,5007/[O II] λ3727 (also known as O32). Given the similarity of the locations in the [O III]/Hβ–[N II]/Hα BPT diagram (Figure 5) among our sample, $z \sim 2$ star-forming galaxies, and the local analogs analyzed in Bian et al. (2018), these empirical calibrations are likely to be useful for these galaxies at $z > 6$. In the absence of statistical samples of strong line ratios above $z > 3$, an estimate using the $z = 0 - 2$ calibrations can provide a valuable first look, but we also make the caveat clear that the empirical calibration may break down in this unexplored redshift regime (e.g., see discussions in Curti et al. 2023 and most recently Sanders et al. 2023b). This is possibly because of the different ISM conditions and physical properties (e.g., N/O, ionization

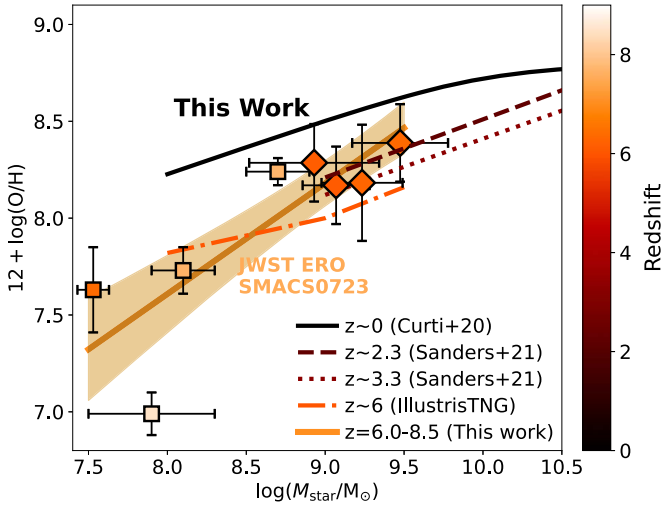

Figure 6. Gas-phase metallicity vs. stellar mass of $z > 6$ galaxies in our sample (diamonds; measured using various strong line ratios calibrated by Bian et al. 2018), compared with those obtained with JWST/NIRSpec early-release observations in SMACSJ0723 field (squares; Taylor et al. 2022; Curti et al. 2023) measured using the direct T_e method. The best-fit mass–metallicity relation of $z > 6$ galaxies is shown as a solid-orange line, with 1σ uncertainty shown as a shallower filled region. We also compare our measurements with those of SDSS galaxies in the local universe (Curti et al. 2020), and $z \sim 2.3$ and 3.3 galaxies in the MOSDEF sample (Sanders et al. 2021; also based on Bian et al. 2018 calibration). Mass-metallicity relation at $z \sim 6$ in the IllustrisTNG simulation (Torrey et al. 2019) is also shown for comparison (dashed–dotted orange–red line). All of the samples and relations shown in this plot are color-coded by the redshifts.

parameter, hardness of the ionizing radiation; Steidel et al. 2016; Strom et al. 2017) of high-redshift galaxies relative to the calibration samples at lower redshifts (Brinchmann 2023).

We derive the gas-phase metallicity of each source by averaging the measurements with multiple tracers, including N2 (P330E-z6.35), R23 (P330E-z6.28 and P330E-z6.35), and [O III]/Hβ (O3; all sources). For sources without Hβ detections, we assume an intrinsic Hα/Hβ ratio of 2.86 (case B recombination and electron temperature of 10^4 K). One caveat is that the Hα/Hβ ratio could be underestimated because of the dust extinction, and the resultant O/H abundance could be overestimated by 0.2 dex if the Hα/Hβ ratio is 4. We estimated the uncertainty of metallicity from both the errors of line ratios and the scattering of measurements with multiple tracers. The derived gas-phase metallicities are reported in Table 1. In general, the galaxies in our sample have been enriched to moderate metallicities ($\sim$0.4 $Z_\odot$).

Figure 6 shows the metallicities versus stellar masses of sources in our sample at $z > 6$. We also compare our measurements with those of the four $z > 6$ galaxies observed through the JWST/NIRSpec ERO of the SMACS0723 field (Pontoppidan et al. 2022). For three sources at $z > 7$, we adopt the stellar-mass measurements from Tacchella et al. (2022, see also Trussler et al. 2023) and gas-phase metallicities from Curti et al. (2023) using the direct T_e method. For the $z = 6.38$ galaxy, we adopt the M_{star} from Carnall et al. (2023) and 12 + log(O/H) from Taylor et al. (2022). We also note that metallicity measurements from Rhoads et al. (2023), Schaerer et al. (2022), Tacchella et al. (2022), and Trump et al. (2023) are in general agreement (Brinchmann 2023). With higher stellar masses and slightly lower redshift, the galaxies in our sample exhibit higher metallicities than those of the four $z > 6$ galaxies in the SMACS0723 field. The best-fit mass–metallicity (gas-phase) relation from these eight sources at $z = 6.0 - 8.5$ is:

$$12 + \log(\mathrm{O/H}) = (0.57 \pm 0.16)\log\left(\frac{M_{\mathrm{star}}}{10^9\ M_\odot}\right) + 8.18 \pm 0.12 \quad (1)$$

which is shown as the solid-orange line in Figure 6, with the lighter filled region indicating the 1σ uncertainty range.

Within the investigated stellar mass range ($M_{star} = 10^{7.5} \sim 10^{9.5}\ M_\odot$), our best-fit relation suggests a lower metallicity at a given stellar mass when compared with $z \sim 0$ galaxies observed with SDSS (e.g., Curti et al. 2020). However, four galaxies in our sample exhibit moderate metallicities that are comparable to those of $z \simeq$ 2–3 galaxies in the MOSDEF sample (Sanders et al. 2021), whose metallicities were also derived based on the Bian et al. (2018) calibration. The observed metallicities of sources in our sample are slightly higher than those of galaxies with similar stellar masses in certain cosmological simulations, including IllustrisTNG (Torrey et al. 2019). As a result, the best-fit mass–metallicity relation at $z > 6$ with JWST is also steeper than that in IllustrisTNG.

However, we note that the slope of the mass–metallicity relation flattens to 0.41 ± 0.07 if the $z = 8.5$ source with extremely low metallicity ($12 + \log(\mathrm{O/H}) = 7.0 \pm 0.1$; Curti et al. 2023) in JWST/NIRSpec ERO is excluded from the linear fitting, which makes the slope closer to those seen at $z \simeq 2 - 3$ ($\sim$0.30, Sanders et al. 2021; see also Li et al. 2022 most recently). We also note that to fully explore the evolution with respect to low-redshift galaxies and compare with simulations, one should also consider the secondary dependence of metallicity on SFR (i.e., the fundamental metallicity relation, see discussion in Curti et al. 2023). This additional step is beyond the scope of this paper.

Our observations may indicate a rapid metal enrichment in certain massive ($M_{star} \gtrsim 10^9\ M_\odot$) galaxies at $z > 6$, which is also suggested by the [O III] 88 μm and dust detections of $z > 8$ galaxies with ALMA (Tamura et al. 2019; see also Jones et al. 2020). The enhanced gas-phase metallicity potentially indicates that the recent increase in SFR is driven by mergers or internal gravitational instabilities (e.g., Tacchella et al. 2022) instead of pristine gas inflow, which can result in lower gas-phase metallicity. Such ancient and rapid metallicity evolution and intense episode of star formation is also in a sense reminiscent of the formation scenario of our own Milky Way Bulge, which indeed rapidly evolved toward solar metallicity and formed most of stellar mass >10 Gyr ago. However, we also note that our metallicity measurements are totally based on the low-redshift strong-line calibrations, mostly in the metallicity range of $7.8 < 12 + \log(\mathrm{O/H}) < 8.4$ (Bian et al. 2018). Further direct gas-phase metallicity measurements through JWST/NIRSpec observations (e.g., most recently with Nakajima et al. 2023 and Sanders et al. 2023b) are necessary for more accurate determination of the mass–metallicity relation in the high-redshift universe.

4.5. Redshift Evolution of Hα Line Equivalent Width

Before the launch of the JWST, the Hα EWs at $z \sim 6$ were poorly probed because [O III] and Hα lines are in the bandwidth of IRAC Channel 1 and 2, respectively. In the left-hand panel of Figure 7, we examine the redshift evolution of Hα EWs of galaxies from $z \simeq 0.5$ to 8 in the literature. For

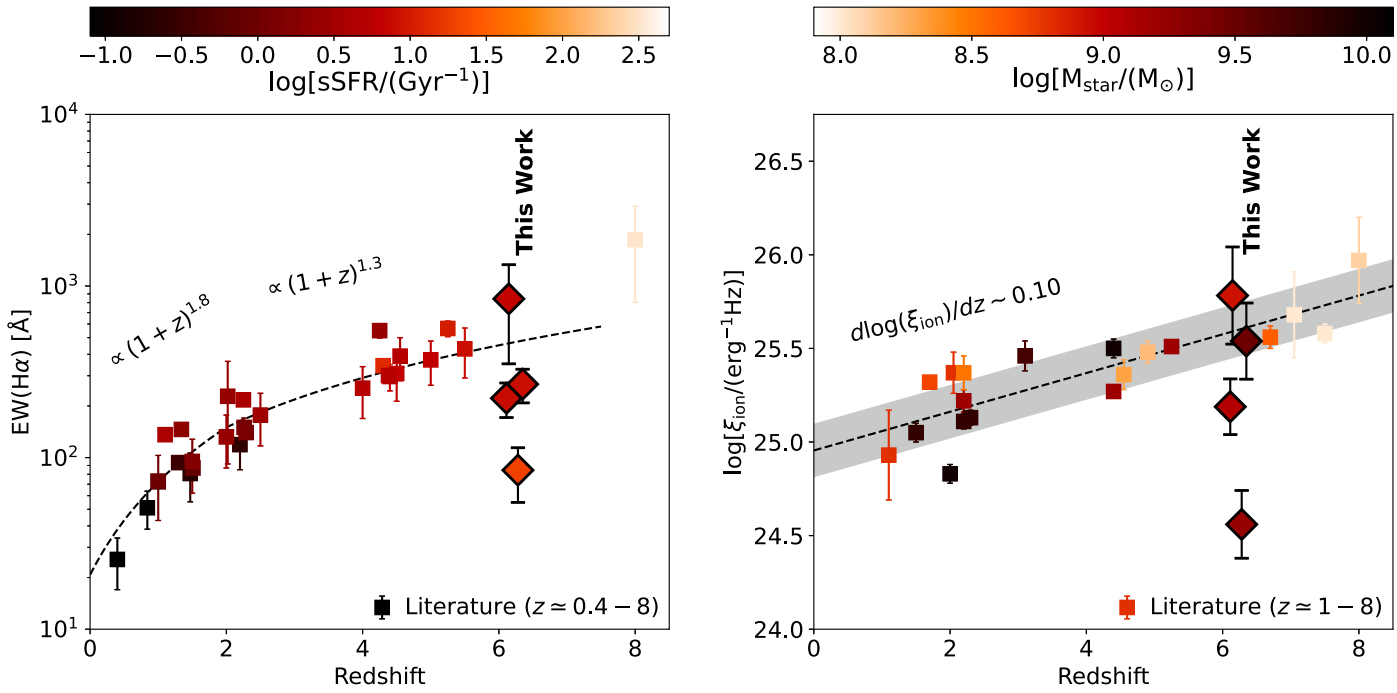

Figure 7. Redshift evolution of Hα equivalent widths (left-hand panel) and ionizing photon production efficiency (right-hand panel) of star-forming galaxies across $z \simeq 0.4$–8. Sources in our sample are shown as diamonds. In the left-hand panel, the reference samples (squares) include Erb et al. (2006), Shim et al. (2011), Fumagalli et al. (2012), Stark et al. (2013), Sobral et al. (2014), Faisst et al. (2016), Mármol-Queraltó et al. (2016), Rasappu et al. (2016), Smit et al. (2016), Reddy et al. (2018), Lam et al. (2019), Atek et al. (2022), Boyett et al. (2022), and Stefanon et al. (2022), and all samples are color-coded by their specific SFRs. The proposed redshift evolution (EW $\propto (1+z)^{1.8}$ at $z < 2$ and $\propto (1+z)^{1.3}$ beyond) in Faisst et al. (2016) is shown as the dashed-black line. In the right-hand panel, the reference samples (squares) include Stark et al. (2015, 2017), Bouwens et al. (2016b), Nakajima et al. (2016), Matthee et al. (2017), Harikane et al. (2018), Shivaei et al. (2018), Faisst et al. (2019), Lam et al. (2019), Tang et al. (2019), Emami et al. (2020), Nanayakkara et al. (2020), Endsley et al. (2021a), Atek et al. (2022), and Stefanon et al. (2022), and all samples are color-coded by their stellar masses. The best-fit redshift evolution ($d \log \xi_{ion}/dz = 0.10 \pm 0.02$) of the literature samples is shown as the dashed-black line, and the 1σ dispersion of the relation (0.14 dex) is indicated by the shaded-gray region.

Hα EW measurements obtained with medium/high-resolution spectroscopy (e.g., Erb et al. 2006; Reddy et al. 2018), we directly use the reported EWs. For measurements with low-resolution grism spectroscopy (e.g., Fumagalli et al. 2012; Atek et al. 2022; Boyett et al. 2022) or narrow-band imaging (Sobral et al. 2014) in which Hα lines are blended with [N II] lines, we assume that 85% of the line fluxes are from Hα, which is consistent with our [N II]/Hα measurements in Section 4.3 (see also recent JWST studies, e.g., Cameron et al. 2023; Helton et al. 2023 and Sanders et al. 2023a). For measurements relying on broadband photometry and SED modeling (e.g., Shim et al. 2011; Stark et al. 2013; Mármol-Queraltó et al. 2016; Rasappu et al. 2016; Smit et al. 2016; Lam et al. 2019; Stefanon et al. 2022), we assume that 80% of Hα+[N II]+[S II] line fluxes are from Hα, which is consistent with the fractions adopted by various studies (71%–84%; e.g., Shim et al. 2011; Rasappu et al. 2016).

The redshift evolution of Hα EWs has been described with EW $\propto (1+z)^{1.8}$ at $z \lesssim 2$ (e.g., Fumagalli et al. 2012) and $\propto (1+z)^{1.3}$ at $z > 2$ (Faisst et al. 2016). At $z > 2.5$, all Hα EWs published before the JWST were derived based on Spitzer/IRAC broadband colors, and therefore are inevitably affected by multiple uncertainties, including the assumption of SFH and dust attenuation. The median EW(Hα) of the sources in our sample is indeed higher than those of $z \lesssim 2$ galaxies with direct spectroscopic measurements and similar to the previous estimates at $z \simeq 4$–5 (e.g., Shim et al. 2011; Stark et al. 2013; Faisst et al. 2016; Mármol-Queraltó et al. 2016; Rasappu et al. 2016; Smit et al. 2016; Lam et al. 2019). This is likely to be a fair comparison because the specific SFRs (sSFR; SFR per unit M_{star}) of these samples are comparable. Note that the Hα EWs broadly reflect the sSFR's of galaxies because Hα is a SFR tracer, while the underlying continuum is related to the luminous stellar mass. However, as the redshifts of galaxies in our sample are higher than those measured with Spitzer/IRAC [3.6]–[4.5] color, this may indicate that the redshift evolution of the Hα EWs is flattening toward the EoR, although the robustness of our conclusion is limited by the small sample size. Finally, our Hα EW measurements are much lower than that of stacked $z \sim 8$ galaxies ($\sim 2 \times 10^3$ Å), as inferred from Spitzer/IRAC [3.6]–[5.8] color (Stefanon et al. 2022), despite a large uncertainty.

4.6. Redshift Evolution of ξ_{ion}

Following a few studies, including Matthee et al. (2017), Shivaei et al. (2018), Tang et al. (2019) and many others, we derive the ionizing photon production efficiency in H II regions as $\xi_{ion} = N(H^0)/L_{UV}$, where $N(H^0)$ is the ionizing photon production rate in the unit of s^{-1}, and L_{UV} is the rest-frame UV luminosity at 1500 Å in the unit of erg s^{-1} Hz^{-1}. The ionizing photon production rate can be computed from the Hα luminosity as $N(H^0) = 7.35 \times 10^{11} L_{H\alpha}$ where $L_{H\alpha}$ is in the unit of erg s^{-1} (Osterbrock & Ferland 2006; Case B recombination at $T_e = 10^4$ K). This is true assuming that the Lyman continuum escape fraction is low ($\lesssim$10%). Note, however, that we do not have near-infrared (1.0–2.2 μm) photometry for our galaxies sampling the rest-frame UV continuum, and therefore we estimate the rest-frame UV luminosities based on the CIGALE modeling performed in the rest-frame optical, as already described.

The median derived $\log[\xi_{\rm ion}/({\rm erg^{-1}\,Hz})]$ of galaxies in our sample is 25.4 ± 0.2, higher than the canonical value of $\sim$25.1 implied by the UV–SFR and Hα–SFR conversion in Kennicutt & Evans (2012). However, a stronger dust attenuation in the rest-frame UV could lead to an overestimate of $\xi_{\rm ion}$. Assuming the Calzetti et al. (2000) extinction law, with an $A_V = 1.0$ and a canonical $E(B-V)$ ratio of 0.44 between stellar continuum and nebular lines, $\xi_{\rm ion}$ would be overestimated by 1.9 times if the dust attenuation is not properly corrected (see also Shivaei et al. 2018).

In the right-hand panel of Figure 7, we study the redshift evolution of the ionization photon production efficiency. The published samples at $z \simeq 1-8$ include Stark et al. (2015, 2017), Bouwens et al. (2016b), Nakajima et al. (2016), Matthee et al. (2017), Harikane et al. (2018), Shivaei et al. (2018), Faisst et al. (2019), Lam et al. (2019), Tang et al. (2019), Emami et al. (2020), Nanayakkara et al. (2020), Endsley et al. (2021a), Atek et al. (2022), and Stefanon et al. (2022). The stellar mass range of the reference sample is $M_{\rm star} \simeq 10^8$–10^{10} $M_\odot$, which is comparable to that of our sample except for those at very high redshifts ($z > 7$). Despite a considerable uncertainty of UV luminosity (because we rely on best-fit SED models) and dust attenuation, the $\xi_{\rm ion}$ measured in this work based on accurate Hα luminosity is consistent with the previous determination at $z \simeq 5-7$ (e.g., Stark et al. 2015; Harikane et al. 2018; Endsley et al. 2021a and most recently Ning et al. 2023 and Tang et al. 2023).

As shown by the dashed-black line in the plot, the published samples indicate a redshift evolution of $\xi_{\rm ion}$ with a slope of $d\log(\xi_{\rm ion})/dz = 0.10 \pm 0.02$ (see also Matthee et al. 2017; Atek et al. 2022 and Stefanon et al. 2022). This redshift evolution can be interpreted by an age effect, i.e., galaxies at higher redshifts have younger stellar populations and therefore higher $\xi_{\rm ion}$ (e.g., Tacchella et al. 2018; Naidu et al. 2020). The galaxies in our sample are in general agreement with such a redshift evolution trend except for P330E-z6.28 ($\log[\xi_{\rm ion}/({\rm erg^{-1}\,Hz})] = 24.6 \pm 0.2$). The large scatter of $\log(\xi_{\rm ion})$ in our sample (0.46 dex; including P330E-z6.28) is also not a surprise because it is also seen in other samples at lower redshifts, which can be propagated from the scatter of dust attenuation, sSFR and patchy ISM coverage (e.g., Matthee et al. 2017; Shivaei et al. 2018).

5. Discussion II: Volume Density

5.1. Emission Line Luminosity Function: Methodology

To compute the LFs of [O III] λ5007 and Hα lines at $z \sim 6.2$, we first compute the total survey volume of [O III]+Hα emitters at $z = 6.0 \sim 6.6$. With the spectral tracing model, dispersion model, and pointing information of the telescope, we compute the maximum survey area in which the direct-imaging sources at $z > 6$ could yield both detectable [O III] and Hα emission lines with the obtained F322W2 and F444W grism observations. The resultant survey area of [O III]+Hα emitters at $z = 6.2$ is shown as the purple contours in Figure 1. The maximum survey area changes from 14.4 arcmin^2 at $z = 6.0$–12.4 arcmin^2 at $z = 6.6$ because the overlapping area that could yield dual line detections decreases toward higher redshifts.

With the maximum survey area, we compute the emission-line LF without a completeness correction, which we refer to as the *uncorrected* LF ($\Phi_{\rm uncorr}$). This reflects the lower limits of Hα and [O III] LF measurements at $z \sim 6.2$ that are directly inferred from the number of source detections ($N_{\rm src}$), maximum survey volume ($V_{\rm max}$ in comoving Mpc^3; assuming $z = 6.0-6.6$), and luminosity bin size ($d\log L$ in the unit of dex) as $\Phi_{\rm uncorr} = N_{\rm src}/(V_{\rm max}\, d\log L)$. The uncorrected LFs of Hα and [O III] λ5007 lines are computed in luminosity bins of $10^{42.4}$–$10^{42.8}$ and $10^{42.8}$–$10^{43.2}$ erg s^{-1}, and Monte Carlo (MC) simulations are performed to quantify the uncertainty propagated from the line flux errors. We also consider the Poisson noise of small number statistics using the prescription of Gehrels (1986). The uncorrected LFs are reported in Table 2.

Table 2
Measured Hα and [O III] λ5007 Line Luminosity Function at $z \sim 6.2$

$\log(L_{\rm line})$ (erg s^{-1})	$N_{\rm src}$	$\log(\Phi_{\rm uncorr})$ (Mpc^{-3} dex^{-1})	$\log(\Phi_{\rm corr})$ (Mpc^{-3} dex^{-1})
[O III] λ5007			
42.6	1	$-4.07^{+0.64}_{-0.76}$	$-2.81^{+0.69}_{-0.89}$
43.0	3	$-3.36^{+0.28}_{-0.32}$	$-3.21^{+0.37}_{-0.41}$
Hα			
42.6	2	$-3.64^{+0.40}_{-0.47}$	$-2.72^{+0.57}_{-0.59}$
43.0	2	$-3.54^{+0.35}_{-0.41}$	$-3.43^{+0.43}_{-0.50}$

Note. Columns: (1) $\log(L_{\rm line})$: Center of emission-line-luminosity bin (bin size: 0.4 dex) in unit of erg s^{-1}; (2) $N_{\rm src}$: Number of sources in the luminosity bin; (3)/(4): uncorrected and corrected volume density of line emitters within the given luminosity bin, respectively (see Section 5.1).

We also compute the line LFs using the direct $1/V_{\rm max}$ method (Schmidt 1968) as:

$$\Phi(L) = \frac{1}{d\log L}\sum_i \frac{1}{C_i V_{{\rm max},i}} \quad (2)$$

where C_i is the completeness of the ith source in the luminosity bin, and $V_{{\rm max},i}$ is the maximum observable volume of the ith source.

The survey completeness is evaluated through MC, which is detailed in the Appendix. In short, we compute the completeness of all line detections by injecting mock line emissions in the 2D spectral image, deriving the line fluxes and errors using the same method as we applied for the real line detections, and evaluating the fraction of realizations above the 3σ detection threshold. We also evaluate the flux-boosting effect and the Eddington bias by comparing injected and output line flux ratios, and correct this for the line luminosities of sources in our sample, which could be boosted by 18% for a S/N = 3 line detection. We also compute the maximum survey volume of each source from the rms error map of the F322W2 and F444W grism images, in which the [O III] λ5007 and Hα lines with the same luminosities as those of the real source can be detected at $\geqslant 3\sigma$. In general, the maximum survey area decreases from $z = 6.0$ to 6.6 because of the increasing rms noise toward the red end of the F444W filter.

We then compute the completeness-corrected line LFs ($\Phi_{\rm corr}$) using the same luminosity bins as those for $\Phi_{\rm uncorr}$. We also employ MC simulations for correct error propagation from line flux to LF and consider Poisson noise for small number statistics as described above for $\Phi_{\rm uncorr}$. Finally, we also consider the impact from the cosmic variance following the simple prescription in Driver & Robotham (2010), which could introduce a further uncertainty of 0.2 dex. Because the

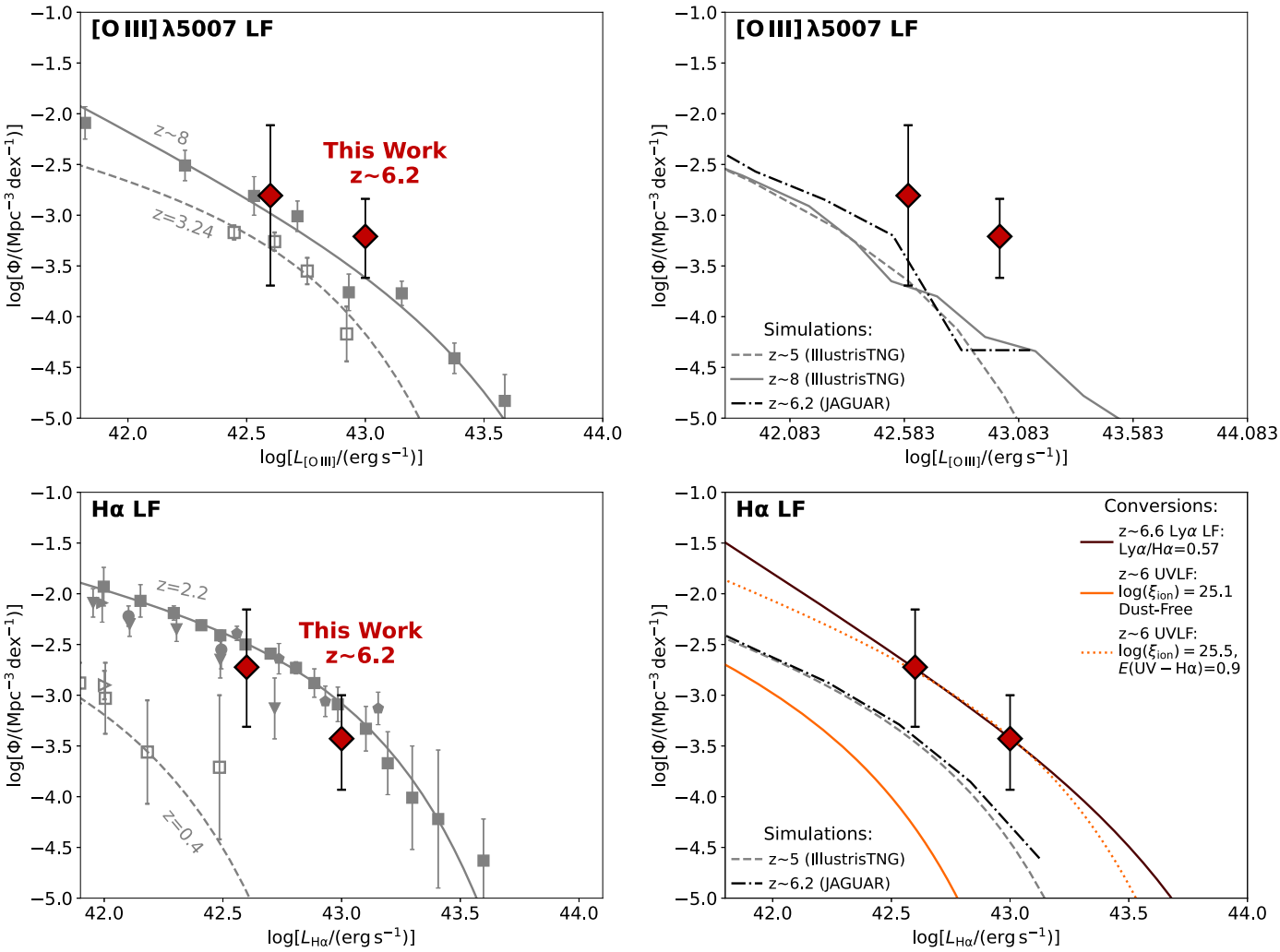

Figure 8. Top left-hand panel: $z \sim 6.2$ [O III] λ5007 line-luminosity function derived in this work (red diamonds). For comparison, we show the $z = 3.24$ [O III] LF measured by Khostovan et al. (2015) through narrow-band imaging (open squares and dashed line), and $z \sim 8$ [O III] LF (De Barros et al. 2019) inferred from the UVLF and Spitzer/IRAC colors (filled squares and solid line). Top right-hand panel: Observed [O III] λ5007 luminosity function compared with those in simulations, including IllustrisTNG at $z = 5$ (dashed-gray line), $z = 8$ (solid-gray line; Shen et al. 2020), and the JAGUAR mock catalog at $z \sim 6.2$ (dashed–dotted black line; Williams et al. 2018). Bottom left-hand panel: $z \sim 6.2$ Hα line-luminosity function derived in this work (red diamonds). For comparison, we show the Hα LF measurements at $z = 2.2$ (Geach et al. 2008; Hayes et al. 2010b; Tadaki et al. 2011; Lee et al. 2012; Sobral et al. 2013) and $z = 0.4$ (Ly et al. 2007; Sobral et al. 2013). Best-fit Schechter functions at $z = 2.2$ and 0.4 (Sobral et al. 2013) are shown as solid- and dashed-gray lines, respectively. Bottom right-hand panel: Observed Hα LF compared with those in simulations (IllustrisTNG at $z \sim 5$, dashed-gray lines, Shen et al. 2020; JAGUAR mock catalog at $z \sim 6.2$, dashed–dotted black line, Williams et al. 2018). We also compare with the $z \sim 6$ UVLF (Bouwens et al. 2021) by converting UV luminosity to Hα luminosity under a constant SFR assumption (Kennicutt & Evans 2012; effectively $\log[\xi_{\rm ion}/({\rm erg^{-1}\,Hz})] = 25.1$ and no dust attenuation), as shown in the solid-orange line. We also perform the conversion assuming an enhanced $\log[\xi_{\rm ion}/({\rm erg^{-1}\,Hz})] = 25.5$ and UV − Hα color excess of 0.9, as shown in the dotted orange line. Conversion from $z \sim 6.6$ Lyα LF (Konno et al. 2018; assuming a line ratio of Lyα/H$\alpha = 0.57$) is shown in the solid-brown line.

galaxies in our sample are confirmed at different redshifts, it is unlikely that our LF measurements are affected by galaxy overdensities, which cluster at specific redshifts.

The corrected LFs are also reported in Table 2. In the bright bin ($L_{\rm line} = 10^{42.8}$–$10^{43.2}$ erg s^{-1}), $\log(\Phi_{\rm corr})$ is higher than the uncorrected value by 0.1–0.2 dex. In the faint bin ($L_{\rm line} = 10^{42.4}$–$10^{42.8}$ erg s^{-1}), the uncorrected LF likely underpredicts the volume density of both Hα and [O III] λ5007 emitters by $\sim$1 dex, although with a large uncertainty ($0.6 \sim 0.9$ dex) because of small number statistics and a large uncertainty propagated from the line flux error. In Figure 8, we display the measured $\log(\Phi_{\rm corr})$ of [O III] λ5007 and Hα line emitters at $z \sim 6.2$, and compared them with other observations and simulations. We note that this is the first time that one could directly measure the LFs of both lines in the EoR, thanks to the unprecedented sensitivity of JWST beyond the K band and unique ability of the NIRCam/Grism WFSS mode to sample line emitters in an unbiased way. However, we are still not able to model the LFs with commonly used formalisms (e.g., Schechter function; Schechter 1976) because of the limited sample size.

5.2. [O III] λ5007 Luminosity Function

The [O III] λ5007 LF at $z \sim 6.2$ is shown in the top left-hand panel of Figure 8. For comparison, we also plot the [O III] λ5007 LF measured by Khostovan et al. (2015) at $z = 3.24$, the highest-redshift [O III] LF measurement that is accessible from the ground using the rest-frame H_2 1–0 S(1) narrow-band filter in the K band (2.12 μm). We also compare our results with the $z \sim 8$ [O III] LF derived by

De Barros et al. (2019) based on the UV LF and the relation between UV and [O III]+Hβ luminosities as inferred from Spitzer/IRAC [3.6]–[4.5] colors. For a fair comparison, we assumed that the [O III] λ5007 line contributes to ∼64% of the total fluxes from Hβ+[O III] lines in the LFs of Khostovan et al. (2015) and De Barros et al. (2019). The adopted value is consistent with the median fraction observed with our sample, which is computed as $f_{[\mathrm{O\,III}]\,5007}/(1.33 f_{[\mathrm{O\,III}]\,5007} + f_{\mathrm{H}\alpha}/2.86)$, assuming the theoretical ratio of 1/3 for [O III] 4959/5007 lines and 2.86 for Hα/Hβ lines.

We find that our [O III] LF measurement at $z \sim 6.2$ is higher than the $z = 3.24$ measurement (Khostovan et al. 2015) by a factor of ∼5, and the scenario of constant [O III] LF can be ruled out from χ^2 statistics (p-value < 0.05). This indicates a strong evolution of [O III] line strength, and therefore possibly of ionization parameter toward higher redshift. Our [O III] LF measurement is also higher than the $z \sim 8$ estimate in De Barros et al. (2019) by a factor of ∼2. From χ^2 statistics, these [O III] LF determinations at $z \sim 6.2$ and ∼8 may be consistent with each other (p-value = 0.3; see also Matthee et al. 2023 for most recent results).

As shown in the top right-hand panel of Figure 8, we also compare our [O III] LF with those predicted by the IllustrisTNG simulation at $z = 5$ and 8 (Shen et al. 2020) and the JAGUAR mock catalog (Williams et al. 2018). These simulations/realizations generally underpredict the observed [O III] λ5007 LF by a factor of ∼10. Because our $\Phi_{\mathrm{corr}}(L)$ measurement of the [O III] LF in the bright bin ($10^{42.8}$–$10^{43.2}$ erg s^{-1}) is based on three sources (instead of only one) and the completeness correction factor is only ∼1.4, we conclude that such a large excess of the [O III] LF compared to those in the simulation is real (see also recent simulations presented by Wilkins et al. 2023). These simulations are typically tuned to match empirical distributions where possible, which in the case of ionization parameter ($\log U$) are best characterized at low redshifts (e.g., the $\log U$–$Z/Z_{\odot}$ relation from Carton et al. 2017, in the case of the JAGUAR mock catalog). This is now known to underpredict rest-frame optical line fluxes such as Hα and [O III] at high redshifts (e.g., De Barros et al. 2019; Maseda et al. 2019) as we find here, which indicates the likely strong evolution that will be revealed by larger samples in upcoming JWST surveys.

5.3. Hα Luminosity Function

In the lower left-hand panel of Figure 8, we first compare our $z \sim 6.2$ Hα LF measurement (uncorrected for dust attenuation) with those at $z \sim 0.4$ (Ly et al. 2007; Sobral et al. 2013; through 921 nm narrow band) and $z \sim 2.2$ (Geach et al. 2008; Hayes et al. 2010b; Tadaki et al. 2011; Lee et al. 2012; Sobral et al. 2013), which are still accessible from the ground using the 2.12 μm narrow-band filter. No direct measurement of Hα LF exists beyond $z \sim 2.2$ before the launch of JWST. We find that the $z \sim 6.2$ Hα LF measured with this work is higher than those at $z \sim 0.4$ but only slightly lower than those at $z \sim 2.2$, which potentially suggests weak or no evolution of Hα LF (p-value = 0.36 from χ^2 statistics) from the end of EoR to the peak of cosmic star formation history ($z \sim 2$, see Madau & Dickinson 2014 for a review). In the context of decreasing cosmic SFR density from $z \sim 2$ to 6, the observed constancy of the Hα LFs between these two epochs possibly indicates: (i) a higher ionizing photon production efficiency at higher redshift (see discussion in Section 4.5 and reference therein), which leads to a higher $L_{\mathrm{H}\alpha}$/SFR ratio in the EoR; and (ii) a decreasing obscured fraction of Hα emission, and therefore decreasing obscured fraction of cosmic SFR density from $z \sim 2$ to 6, as shown in recent ALMA dust-continuum source surveys (e.g., Bouwens et al. 2020; Casey et al. 2021; Zavala et al. 2021; Sun et al. 2022a).

In the lower right-hand panel of Figure 8, we show that our $z \sim 6.2$ Hα LF measurement is 6–8 times higher than those predicted in the IllustrisTNG simulation ($z \sim 5$; Shen et al. 2020) and JAGUAR mock catalog ($z \sim 6.2$; Williams et al. 2018), similar to the [O III] LF. As discussed in Section 5.2, this reflects our limited understanding of the rest-frame optical emission-line strength of $z \gtrsim 6$ galaxies before the launch of JWST. This is likely to be caused by the underestimate of ionizing luminosities for $z \gtrsim 6$ galaxies with subsolar metallicities (Williams et al. 2018), such as those in our sample.

In addition, if we simply translate the $z \sim 6$ UV LF (e.g., Bouwens et al. 2021) to Hα LF assuming the constant SFR conversions in Kennicutt & Evans (2012), then the volume density of Hα emitters would be underpredicted by ∼100 times at $L_{\mathrm{H}\alpha} > 10^{42.6}$ erg s^{-1}. This suggests that: (i) the dust attenuation is still substantial for UV-luminous galaxies even at $z > 6$, as is shown in recent ALMA studies (e.g., Inami et al. 2022; Schouws et al. 2022; Algera et al. 2023), despite a decreasing volume density of obscured SFR; and (ii) an enhanced ξ_{ion} at high redshift when compared with the local universe. If we assume a typical $\log[\xi_{\mathrm{ion}}/(\mathrm{erg^{-1}\,Hz})] = 25.5$ for galaxies at $z \sim 6$ (see Section 4.6), then the observed Hα LF can be well matched to the conversion from the UV LF with a color excess of $E(\mathrm{UV} - \mathrm{H}\alpha) = 0.9 \pm 0.5$. This can be translated to an $E(B-V) = 0.33 \pm 0.18$ and $A_V = 1.3 \pm 0.7$ assuming Calzetti et al. (2000) extinction law, and also $E(B-V) = 0.11 \pm 0.06$ and $A_V = 0.30 \pm 0.17$ assuming the SMC extinction law of Gordon et al. (2003), both adopting the canonical $E(B-V)$ ratio of 0.44 between stellar continuum and nebular lines (Calzetti et al. 2000).

5.4. Implication for the Global Lyα Escape Fraction

As shown in the lower right-hand panel of Figure 8, our observed Hα LF can match the observed Lyα LF at $z = 6.6$ (Konno et al. 2018) assuming a Lyα/Hα flux ratio of $0.57^{+0.35}_{-0.22}$. We note that this also assumes that both Lyα and Hα emission is from the same population of star-forming galaxies. The best match to the Lyα LF at $z = 5.7$ (also Konno et al. 2018) would indicate a Lyα/Hα flux ratio of $0.81^{+0.44}_{-0.28}$. Considering a theoretical Lyα/Hα flux ratio of 8.7 from Case B recombination (see Hayes et al. 2011 and Henry et al. 2015) and assuming no evolution of Hα LF from $z = 5.7$ to 6.6, this suggests a global Lyα escape fraction ($f^{\mathrm{esc}}_{\mathrm{Ly}\alpha} = f(\mathrm{Ly}\alpha)/f(\mathrm{H}\alpha)/8.7$) of $6.5^{+4.0}_{-2.4}$% at $z \sim 6.6$ and $9.3^{+5.0}_{-3.2}$% at $z \sim 5.7$. This is consistent with recent JWST measurements of $f^{\mathrm{esc}}_{\mathrm{Ly}\alpha}$ based on Lyα-selected galaxies at $z \sim 6$ (Ning et al. 2023). Note that these values are computed from the observed Hα LF and the intrinsic Hα LF at $z \sim 6.2$ could be even higher because of the dust extinction correction, which may lead to a potential overestimate of $f^{\mathrm{esc}}_{\mathrm{Ly}\alpha}$.

As shown in Figure 9, both values of $f^{\mathrm{esc}}_{\mathrm{Ly}\alpha}$ are consistent with the global Lyα escape fraction found at $z \sim 2.2$ through the direct comparison of Lyα/Hα LFs (e.g., Hayes et al. 2010a; Sobral et al. 2017), but only ∼1/4 of the early measurement of $f^{\mathrm{esc}}_{\mathrm{Ly}\alpha}$ at $z \sim 6$ in Hayes et al. (2011, ∼30%) and ∼1/2 of that in Konno et al. (2016, ∼15%). As discussed in Konno et al.

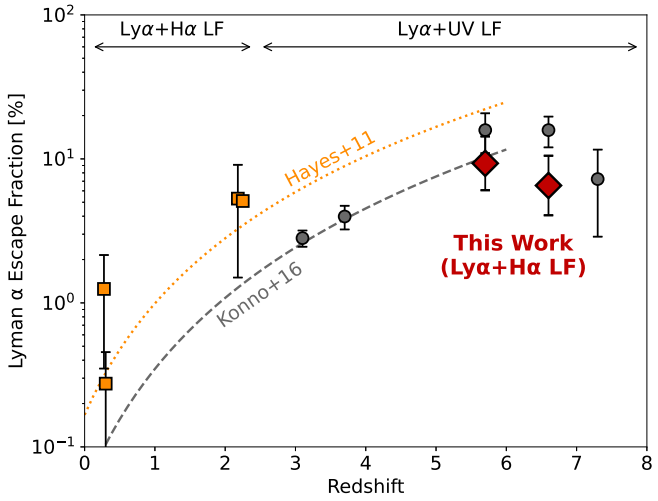

Figure 9. Global escape fraction of Lyα photons vs. redshift. Lyα escape fraction at $z = 5.7$ and 6.6 based on Lyα LF in Konno et al. (2018) and Hα LF measured in this work are shown as red diamonds (see Section 5.3). $z \simeq 0.2$–2.2 measurements using Lyα and Hα LFs are shown as orange squares (Deharveng et al. 2008; Cowie et al. 2010; Hayes et al. 2010a, 2011; Sobral et al. 2017), and the best-fit relation for the $z \simeq 0$–6 compilations in Hayes et al. (2011) is shown as the dotted orange line. $z \simeq 3$–8 measurements using Lyα and UV LFs compiled by Konno et al. (2016) are shown as gray circles and the best-fit relation for their $z \simeq 0$–6 compilation is shown as the dashed-gray line.

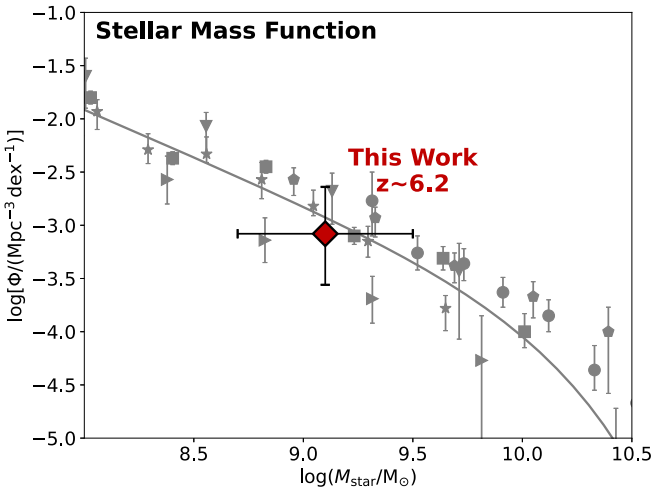

Figure 10. Comparison with galaxy stellar-mass function at $z \sim 6$ (Duncan et al. 2014, pentagons; Grazian et al. 2015, circles; Song et al. 2016, rightward triangles; Bhatawdekar et al. 2019, downward triangles; Kikuchihara et al. 2020, stars; Stefanon et al. 2021, squares). Compared with the best-fit Schechter function in Stefanon et al. (2022), as shown in the solid-gray line, our sample recovers 88^{+164}_{-57}% of $z \sim 6$ galaxies with stellar mass above $5 \times 10^8\ M_\odot$.

(2016), the difference in measured $f_{\rm Ly\alpha}^{\rm esc}$ between Hayes et al. (2011) and Konno et al. (2016) is mainly from the different lower limits of Lyα and UV luminosities for the integration of their densities. In the previous literature, the estimate of Lyα escape fraction at $z > 2.2$ relied on the conversion between UV and Hα SFR because direct Hα luminosity measurement was impossible from the ground. However, the Hα luminosity could be underestimated from SFR with the classical Kennicutt & Evans (2012) conversion because of an enhanced $\xi_{\rm ion}$ at higher redshift, leading to an overestimated Lyα escape fraction (see also Matthee et al. 2022; Naidu et al. 2022).

Our measurement further suggests no or weak evolution of Lyα escape fraction at $z \simeq 2-6$, in contrast to previous estimates that generally predict a $f_{\rm Ly\alpha}^{\rm esc} \propto (1+z)^{2.6} \sim (1+z)^{2.8}$ evolution (see Hayes et al. 2011; Konno et al. 2016 and a review by Ouchi et al. 2020). Despite this, the general picture of declining $f_{\rm Ly\alpha}^{\rm esc}$ at $z > 6$ when compared with those at $z = 3.1$ and 5.7 (e.g., Konno et al. 2016, 2018) would still remain valid, which is consistent with the increasing neutral fraction of intergalactic medium at higher redshifts. A more solid assessment would come in the future by obtaining Lyα spectroscopy of the same targets, which could provide direct information on the Lyα/Hα line ratio.

5.5. Biases and Comparison with Stellar Mass Function

The selection of both [O III] λ5007 and Hα emitters could potentially bias our sample toward the high-metallicity end of emission-line galaxies at $z > 6$ because metal-poor galaxies could have a lower [O III]/Hα flux ratio (e.g., Harikane et al. 2018), and therefore the [O III] line could be fainter than the detection limit. Meanwhile, the requirement of Hα detection can also bias our sample toward sources with higher instantaneous SFR, and therefore younger stellar population, and sources with high [O III] luminosities (higher ionization parameters) but low Hα luminosities can be potentially missed. In addition, the detection of line emitters requires the detection in direct-imaging data, i.e., brighter than $\sim$25 AB mag in either the F322W2 or F444W bands. This means that for a source with comparable line fluxes, such as those in our sample, it would not make the selection if the stellar mass was $\sim$0.5 dex lower, leading to a selection bias against sources with large EWs (e.g., Maseda et al. 2018).

Bearing all of these potential biases in mind, we compare the volume densities of galaxies in our sample (using $1/V_{\rm max}$ method as in Section 5.1) with those of $z \sim 6$ galaxies with the similar stellar masses in Figure 10. The published samples include measurements from Duncan et al. (2014), Grazian et al. (2015), Song et al. (2016), Bhatawdekar et al. (2019), Kikuchihara et al. (2020), and Stefanon et al. (2021), and all their stellar masses have been converted to those with Chabrier (2003) IMF. With a mean stellar mass of $1.4^{+0.7}_{-0.5} \times 10^9\ M_\odot$, the total volume density of galaxies in our sample is $10^{-3.1\pm0.5}$ Mpc^{-3} dex^{-1}. Such a volume density is derived assuming a stellar-mass bin from $4 \times 10^8 \sim 4 \times 10^9\ M_\odot$. We also consider the error of stellar-mass measurements and small number statistics through MC simulation (similar to Section 5.1).

The volume density of emission-line galaxies in our sample is $0.7^{+1.2}_{-0.5}$ times the volume density of $z \sim 6$ galaxies with comparable stellar masses as measured in Stefanon et al. (2021) using their best-fit Schechter function. By integrating the stellar-mass function in Stefanon et al. (2021), we find that our sample recovers 66^{+128}_{-44}% of the $z \simeq 6.0-6.6$ galaxies in the effective survey volume with stellar masses greater than $5 \times 10^8\ M_\odot$. Such a high fraction of recovery suggests that our sample well represents a reasonably large subsample of $z \sim 6$ galaxies with $M_{\rm star} \sim 10^9\ M_\odot$, and the emission-line galaxies are ubiquitous within such stellar mass and redshift ranges.

6. Summary

We present a sample of four Hα+[O III] λ5007 line emitters at $z = 6.11-6.35$ that were discovered through JWST/NIRCam WFSS observations obtained during the

commissioning phase. Located in the field of the flux calibrator P330-E, all four galaxies in our sample were spectroscopically confirmed with robust detections of Hα ($>3\sigma$) and [O III] λ5007 lines ($>5\sigma$), including the one at $z = 6.11$ that has already been reported in Sun et al. (2022a, Paper I). [O II] λ3727 and [O III] λ4959 lines were also tentatively identified for a few sources. With the spectroscopic and photometric measurements obtained with JWST/NIRCam, we performed SED modeling, and analyzed their physical properties and volume densities. The main results follow:

1. The median Hβ+[O III] line EW of galaxies in our sample is 416 ± 66 Å, which is consistent with those inferred previously at $z \simeq 6.7 - 7.0$ from Spitzer/IRAC SED analysis (e.g., Endsley et al. 2021a, 2021b). The median Hα line EW is 239 ± 45 Å, which is smaller than those inferred previously at $z \simeq 5.1 - 5.4$ in Rasappu et al. (2016, also from IRAC SED analysis). All [O III] and Hα EWs of these $z > 6$ galaxies are much larger than those in the local universe with similar stellar masses.
2. The sources in our sample likely occupy the same parameter space as that of $z \sim 2$ star-forming galaxies in the [O III]/Hβ–[N II]/Hα BPT diagram, but are located above the star-forming sequence of local galaxies in the diagram. This could be explained by their elevated N/O abundance at a given O/H ratio, and/or higher ionization parameters, like those seen with $z \sim 2$ galaxies.
3. Through the strong-line ratios, we show that these $z > 6$ galaxies have been enriched to moderate metallicities ($\sim 0.4\, Z_\odot$), comparable to those of galaxies at $z = 2 - 3$ with similar stellar masses. Combined with the direct metallicity measurements of low-mass galaxies obtained from the JWST/NIRSpec ERO data, we find a steep slope of the mass–metallicity relation in the EoR. This may indicate a rapid metallicity enrichment history in certain massive ($M_{\rm star} \gtrsim 10^9\, M_\odot$) galaxies at $z > 6$.
4. The median Hα EW of galaxies in our sample is higher than that of star-forming galaxies at $z \lesssim 2$, but is consistent with that at $z \simeq 4 - 5$ inferred previously. This may indicate a flattening of the redshift evolution of Hα EWs toward the EoR.
5. The galaxies in our sample have a median ionizing photon production efficiency of $\log[\xi_{\rm ion}/({\rm erg^{-1}\,Hz})] = 25.4 \pm 0.2$. Even with some uncertainty associated with dust attenuation correction, this value appears to be consistent with the redshift evolution trend in previous studies where $d\log(\xi_{\rm ion})/dz = 0.10 \pm 0.02$. A higher $\xi_{\rm ion}$ at higher redshift can lead to a higher Hα-based SFR estimate when compared to that derived from UV if the canonical conversion factors are used (e.g., Kennicutt & Evans 2012).
6. We derived the [O III] λ5007 and Hα line LFs using the $1/V_{\rm max}$ method. This is the first time that these two line LFs can be directly measured in the EoR. The $z \sim 6.2$ [O III] LF that we measured is higher than those measured previously at $z = 3.24$ (Khostovan et al. 2015), but likely consistent with that inferred at $z \sim 8$ (De Barros et al. 2019). It is also higher than those in the IllustrisTNG simulation (Shen et al. 2020) and JAGUAR mock catalog (Williams et al. 2018) at comparable redshift by $\sim$10 times.
7. Our measurements suggest weak or no evolution with the Hα line LF from $z \sim 2$ to 6. The measured Hα LF at $z \sim 6$ exceeds the predictions from certain previous simulations/realizations by a factor of 6–8. A simple conversion from the $z \sim 6$ UV LF assuming SFR(Hα) = SFR(UV) would underpredict Hα LF (at $L_{\rm H\alpha} > 10^{42.6}$ erg s^{-1}) by a factor of $\sim$100. This suggests an enhanced ionizing photon production efficiency and a substantial dust attenuation for UV-luminous galaxies at $z \sim 6$.
8. By directly comparing the Lyα and Hα LF at $z \sim 6$, we find a global Lyα escape fraction of $9.3^{+5.0}_{-3.2}$% at $z = 5.7$ and $6.5^{+4.0}_{-2.4}$% at $z = 6.6$. In contrast to previous studies that used UV-based SFR to infer Hα, and therefore intrinsic Lyα luminosity, our study suggests no or weak evolution of the Lyα escape fraction at $z \simeq 2 - 6$. Despite this, the general picture of declining $f^{\rm esc}_{\rm Ly\alpha}$ at $z > 6$ should still remain valid.
9. Despite some potential biases inherent in our selection of [O III]+Hα emitters, the four galaxies in our sample have already contributed to a volume density of $10^{-3.1\pm0.5}$ Mpc^{-3} dex^{-1}. This means that our sample recovers 66^{+128}_{-44}% of the $z = 6.0 - 6.6$ galaxies within the effective survey volume with $M_{\rm star} > 5 \times 10^8\, M_\odot$. Such a high recovery fraction indicates a low selection bias of our sample, as well as the ubiquity of emission-line galaxies within such stellar-mass and redshift ranges.

Acknowledgments

We thank the anonymous referee for their helpful comments. F.S. thanks Fuyan Bian, Zheng Cai, Daniel Ceverino and Daniel P. Stark for helpful discussions. F.S., E.E., M.R., D.J.E., D.K., C.C.W., and C.N.A.W. acknowledge funding from JWST/NIRCam contract to the University of Arizona, NAS5-02105. A.J.B. acknowledges funding from the "First-Galaxies" Advanced Grant from the European Research Council (ERC) under the European Union's Horizon 2020 research and innovation program (grant agreement No. 789056).

This work is based on observations made with the NASA/ESA/CSA James Webb Space Telescope. The data were obtained from the Mikulski Archive for Space Telescopes at the Space Telescope Science Institute, which is operated by the Association of Universities for Research in Astronomy, Inc., under NASA contract NAS 5-03127 for JWST. These observations are associated with program #1076. This paper is based upon High Performance Computing (HPC) resources supported by the University of Arizona TRIF, UITS, and Research, Innovation, and Impact (RII) and maintained by the UArizona Research Technologies department. All of the data presented in this paper were obtained from the Mikulski Archive for Space Telescopes (MAST) at the Space Telescope Science Institute. The specific observations analyzed can be accessed via 10.17909/f8p1-e696.

Facility: JWST (NIRCam).

Software: ASTROPY (Astropy Collaboration et al. 2018), SOURCE EXTRACTOR (Bertin & Arnouts 1996), PHOTUTILS (Bradley et al. 2020), CIGALE (Boquien et al. 2019).

Appendix
Completeness and Effective Survey Volume

A.1. Completeness

To compute the completeness of all [O III] λ5007 and Hα line detections, we first select faint continuum sources

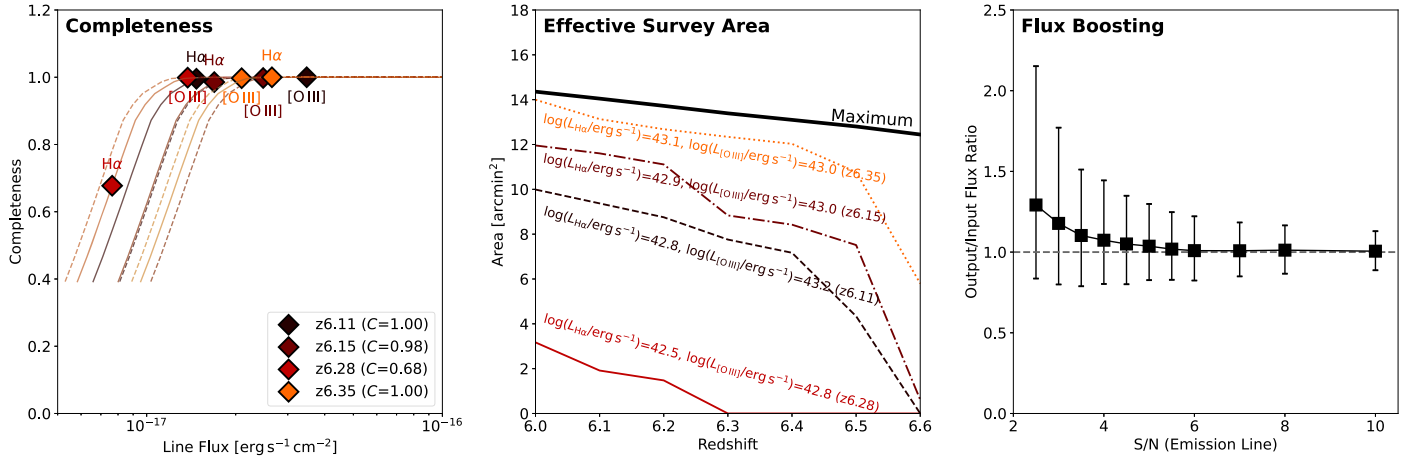

Figure A1. Left-hand panel: Completeness of line emission detection. For each source at $z = 6.11 - 6.35$, we show the simulated completeness as a function of input line flux according to the depth of their observation setup. Completeness functions for Hα and [O III] lines are shown as solid and dashed curves, respectively. The synthesized completeness of line detections for each source is shown in the figure legend. Middle panel: Effective survey area as a function of redshift. The maximum survey area is shown as the solid-black line, and the effective survey areas for the four sources in our sample are shown as colored curves computed from the measured line luminosities. Right-hand panel: Flux-boosting effect (output/input line flux ratio) as a function of input line S/N modeled in our Monte Carlo simulation. The error bars represent the 16th and 84th percentiles of the output flux ratios for each realization.

(F444W > 24 AB mag) for which the grism observations yielded similar spectral coverages as those of the $z > 6$ line emitters. These continuum sources were observed with the same numbers of integrations with each module/grism combination (AR, BR, AC, and BC) at the wavelength of interest (i.e., [O III] λ5007 and Hα wavelengths at $z \sim 6.2$) as those of each line emitter, respectively. However, these F444W sources have no continuum or line emission detected in the grism data.

We then extract and coadd their 2D spectral image, and inject mock line emissions randomly at the same wavelength range of [O III] λ5007 and Hα lines at $z = 5.9 - 6.4$. No mock line emissions are injected at $z > 6.4$ [O III]/Hα wavelengths. This is because the observed Hα wavelengths at these redshifts are too close to the red end of the F444W filter, and therefore the number of coadded integrations can decrease significantly in the 2D spectral images of these faint continuum sources, resulting in jumps of rms noise. The injected line emissions are represented as 2D Gaussian profiles with FWHM $= 5 \sim 6$ pixel in both directions, similar to those of the sources in our sample. The line fluxes and errors are measured using the same method as we applied for the real line detections. The injected line emissions are at various strengths that yield detections at significance levels, ranging from 2σ to 100σ.

Based on the median output line flux errors, we are able to derive the fraction of $\geqslant 3\sigma$ detections for each of the [O III]/Hα line fluxes in our sample, which is the completeness of each line detection. In reality, we find that the fraction of $\geqslant 3\sigma$ detections is well correlated with the S/N of input line, which is defined as the input line flux divided by the median output line flux error. For injected line emissions with input S/N of 5, the completeness of 3σ detection is 97%. However, this decreases to 58% for injected emission lines with a input S/N of 3. Such a completeness function of input line S/N is used to compute the completeness of line detections in our sample. The left-hand panel of Figure A1 shows the completeness of all line detections as a function of the line fluxes. Except for the Hα line of P330E-z6.28 that has a completeness of $\sim$60%, the completeness of all of the other lines are close to 100%. The synthesized completeness is computed as the product of [O III] and Hα line completeness, which is given in the lower right-hand corner of the same panel.

A.2. Survey Volume

The maximum survey volume of each source in our sample is computed from the rms map of F322W2 and F444W grism images. We first measure the rms noise (unit: DN/s) of individual grism integrations taken with each of the four module/grism combinations in both F322W2 and F444W band, respectively. We then constructed the mosaicked rms maps for grism images based on the measured noises and the pointing information of the telescope. We are then able to convert these to the maps of 3σ detection threshold for [O III] and Hα line luminosities at $z = 6.0 \sim 6.6$ using (i) the sensitivity curves of four module/grism combinations in F322W2/F444W filter, and (ii) the relation between the rms noise of 2D spectral image and the median line flux error obtained from the simulations described above. For each source in our sample, we compute the overlapping area from $z = 6.0$ to $z = 6.6$ at a step of $\Delta z = 0.1$, where both their [O III] and Hα line luminosities are above the detection threshold.

The maximum survey areas for all four sources in our sample as functions of redshift are shown in the middle panel of Figure A1. With the lowest Hα and [O III] luminosities, source P330E-z6.28 can only be detected in the deepest 1–2 arcmin^2 area of the survey that contains the flux calibrator, which is consistent with what we observed. The maximum survey volume is then integrated from the maximum survey area across $z = 6.0 - 6.6$. We also run MC simulations to quantify the errors of maximum survey volume propagated from the uncertainty of line flux, which is small ($\sim$5%) for luminous emitters such as P330E-z6.35 but large ($\sim$100%) for faint emitters such as P330E-z6.28. We also consider the reduction of maximum survey volume caused by the existence of bright continuum sources in the field. We conclude that the bright continuum contamination will only result in a small reduction ($\lesssim$5%) of maximum survey volume from visual inspection of the extracted spectra of the faint continuum sources (F444W $\gtrsim 24$ AB mag) because both R and C grism data are available and the field is sparse of bright stars (galactic latitude

$b = +42°$). Such a small reduction is not worthy of correction when compared with the large uncertainty from small number statistics.

A.3. Flux Boosting and Eddington Bias

The flux measurements of low-significance emission lines often suffer from the flux-boosting effect because the Gaussian line-profile fitting routine always searches for the peak of the signal and returns a positive flux. If uncorrected, this will result in an overestimate of the volume density of luminous sources, also known as the Eddington bias (Eddington 1913). The flux-boosting effect is quantified by comparing the injected and output line fluxes at input line S/N from 2 to 100 (Appendix A.1). For each input line S/N, we study the 16–50–84th percentiles of the output/input line flux ratios, which is shown as the right-hand panel of Figure A1. Such a flux-boosting effect is corrected for our line luminosity and LF measurements, and the line luminosity could be boosted by 18% for a $S/N = 3$ detection but only 5% at $S/N = 5$. This is also the reason why 58% of lines with input $S/N = 3$ are actually detected at $S/N \geqslant 3$, instead of 50%, as described in Appendix A.1.

ORCID iDs

Fengwu Sun https://orcid.org/0000-0002-4622-6617
Eiichi Egami https://orcid.org/0000-0003-1344-9475
Nor Pirzkal https://orcid.org/0000-0003-3382-5941
Marcia Rieke https://orcid.org/0000-0002-7893-6170
Stefi Baum https://orcid.org/0000-0002-4735-8224
Martha Boyer https://orcid.org/0000-0003-4850-9589
Kristan Boyett https://orcid.org/0000-0003-4109-304X
Andrew J. Bunker https://orcid.org/0000-0002-8651-9879
Alex J. Cameron https://orcid.org/0000-0002-0450-7306
Mirko Curti https://orcid.org/0000-0002-2678-2560
Daniel J. Eisenstein https://orcid.org/0000-0002-2929-3121
Mario Gennaro https://orcid.org/0000-0002-5581-2896
Thomas P. Greene https://orcid.org/0000-0002-8963-8056
Daniel Jaffe https://orcid.org/0000-0003-3577-3540
Anton M. Koekemoer https://orcid.org/0000-0002-6610-2048
Nimisha Kumari https://orcid.org/0000-0002-5320-2568
Roberto Maiolino https://orcid.org/0000-0002-4985-3819
Michael Maseda https://orcid.org/0000-0003-0695-4414
Michele Perna https://orcid.org/0000-0002-0362-5941
Armin Rest https://orcid.org/0000-0002-4410-5387
Brant E. Robertson https://orcid.org/0000-0002-4271-0364
Everett Schlawin https://orcid.org/0000-0001-8291-6490
Renske Smit https://orcid.org/0000-0001-8034-7802
John Stansberry https://orcid.org/0000-0003-2434-5225
Ben Sunnquist https://orcid.org/0000-0003-3759-8707
Sandro Tacchella https://orcid.org/0000-0002-8224-4505
Christina C. Williams https://orcid.org/0000-0003-2919-7495
Christopher N. A. Willmer https://orcid.org/0000-0001-9262-9997

References

Abazajian, K. N., Adelman-McCarthy, J. K., Agüeros, M. A., et al. 2009, ApJS, 182, 543
Algera, H. S. B., Inami, H., Oesch, P. A., et al. 2023, MNRAS, 518, 6142
Anders, P., Fritze, v., & Alvensleben, U. 2003, A&A, 401, 1063
Arellano-Córdova, K. Z., Berg, D. A., Chisholm, J., et al. 2022, ApJL, 940, L23
Astropy Collaboration, Price-Whelan, A. M., & Sipőcz, B. M. 2018, AJ, 156, 123
Atek, H., Furtak, L. J., Oesch, P., et al. 2022, MNRAS, 511, 4464
Baldwin, J. A., Phillips, M. M., & Terlevich, R. 1981, PASP, 93, 5
Bertin, E., & Arnouts, S. 1996, A&AS, 117, 393
Bhatawdekar, R., Conselice, C. J., Margalef-Bentabol, B., & Duncan, K. 2019, MNRAS, 486, 3805
Bian, F., Kewley, L. J., & Dopita, M. A. 2018, ApJ, 859, 175
Boquien, M., Burgarella, D., Roehlly, Y., et al. 2019, A&A, 622, A103
Bouwens, R., González-López, J., Aravena, M., et al. 2020, ApJ, 902, 112
Bouwens, R. J., Oesch, P. A., Labbé, I., et al. 2016a, ApJ, 830, 67
Bouwens, R. J., Oesch, P. A., Stefanon, M., et al. 2021, AJ, 162, 47
Bouwens, R. J., Smit, R., Labbé, I., et al. 2016b, ApJ, 831, 176
Boyer, M. L., Anderson, J., Gennaro, M., et al. 2022, RNAAS, 6, 191
Boyett, K., Mascia, S., Pentericci, L., et al. 2022, ApJL, 940, L52
Bradley, L., Sipőcz, B., Robitaille, T., et al. 2020, astropy/photutils: 1.0.0, v1.0.0, Zenodo, doi:10.5281/zenodo.4044744
Brinchmann, J. 2023, MNRAS, in press
Brinchmann, J., Charlot, S., White, S. D. M., et al. 2004, MNRAS, 351, 1151
Bruzual, G., & Charlot, S. 2003, MNRAS, 344, 1000
Calzetti, D., Armus, L., Bohlin, R. C., et al. 2000, ApJ, 533, 682
Cameron, A. J., Saxena, A., Bunker, A. J., et al. 2023, arXiv:2302.04298
Carnall, A. C., Begley, R., McLeod, D. J., et al. 2023, MNRAS, 518, L45
Carton, D., Brinchmann, J., Shirazi, M., et al. 2017, MNRAS, 468, 2140
Casey, C. M., Zavala, J. A., Manning, S. M., et al. 2021, ApJ, 923, 215
Ceverino, D., Hirschmann, M., Klessen, R. S., et al. 2021, MNRAS, 504, 4472
Chabrier, G. 2003, PASP, 115, 763
Charlot, S., Kauffmann, G., Longhetti, M., et al. 2002, MNRAS, 330, 876
Cowie, L. L., Barger, A. J., & Hu, E. M. 2010, ApJ, 711, 928
Curti, M., D'Eugenio, F., Carniani, S., et al. 2023, MNRAS, 518, 425
Curti, M., Hayden-Pawson, C., Maiolino, R., et al. 2022, MNRAS, 512, 4136
Curti, M., Mannucci, F., Cresci, G., & Maiolino, R. 2020, MNRAS, 491, 944
De Barros, S., Oesch, P. A., Labbé, I., et al. 2019, MNRAS, 489, 2355
Deharveng, J.-M., Small, T., Barlow, T. A., et al. 2008, ApJ, 680, 1072
Driver, S. P., & Robotham, A. S. G. 2010, MNRAS, 407, 2131
Duncan, K., Conselice, C. J., Mortlock, A., et al. 2014, MNRAS, 444, 2960
Eddington, A. S. 1913, MNRAS, 73, 359
Egami, E., Kneib, J. P., Rieke, G. H., et al. 2005, ApJL, 618, L5
Emami, N., Siana, B., Alavi, A., et al. 2020, ApJ, 895, 116
Endsley, R., Stark, D. P., Charlot, S., et al. 2021a, MNRAS, 502, 6044
Endsley, R., Stark, D. P., Chevallard, J., & Charlot, S. 2021b, MNRAS, 500, 5229
Erb, D. K., Steidel, C. C., Shapley, A. E., et al. 2006, ApJ, 647, 128
Faisst, A. L., Capak, P., Hsieh, B. C., et al. 2016, ApJ, 821, 122
Faisst, A. L., Capak, P. L., Emami, N., Tacchella, S., & Larson, K. L. 2019, ApJ, 884, 133
Fumagalli, M., Patel, S. G., Franx, M., et al. 2012, ApJL, 757, L22
Gaia Collaboration, Brown, A. G. A., Vallenari, A., et al. 2018, A&A, 616, A1
Gardner, J. P., Mather, J. C., Abbott, R., et al. 2023, PASP, 135, 068001
Geach, J. E., Smail, I., Best, P. N., et al. 2008, MNRAS, 388, 1473
Gehrels, N. 1986, ApJ, 303, 336
Gordon, K. D., Bohlin, R., Sloan, G. C., et al. 2022, AJ, 163, 267
Gordon, K. D., Clayton, G. C., Misselt, K. A., Landolt, A. U., & Wolff, M. J. 2003, ApJ, 594, 279
Grazian, A., Fontana, A., Santini, P., et al. 2015, A&A, 575, A96
Greene, T. P., Kelly, D. M., Stansberry, J., et al. 2017, JATIS, 3, 035001
Harikane, Y., Ouchi, M., Shibuya, T., et al. 2018, ApJ, 859, 84
Hayes, M., Östlin, G., Schaerer, D., et al. 2010a, Natur, 464, 562
Hayes, M., Schaerer, D., & Östlin, G. 2010b, A&A, 509, L5
Hayes, M., Schaerer, D., Östlin, G., et al. 2011, ApJ, 730, 8
Helton, J. M., Sun, F., Woodrum, C., et al. 2023, arXiv:2302.10217
Henry, A., Scarlata, C., Martin, C. L., & Erb, D. 2015, ApJ, 809, 19
Horne, K. 1986, PASP, 98, 609
Inami, H., Algera, H. S. B., Schouws, S., et al. 2022, MNRAS, 515, 3126
Jones, T., Sanders, R., Roberts-Borsani, G., et al. 2020, ApJ, 903, 150
Katz, H., Saxena, A., Cameron, A. J., et al. 2023, MNRAS, 518, 592
Kauffmann, G., Heckman, T. M., Tremonti, C., et al. 2003a, MNRAS, 346, 1055
Kauffmann, G., Heckman, T. M., White, S. D. M., et al. 2003b, MNRAS, 341, 33
Kennicutt, R. C., & Evans, N. J. 2012, ARA&A, 50, 531
Kewley, L. J., Dopita, M. A., Leitherer, C., et al. 2013, ApJ, 774, 100
Kewley, L. J., Dopita, M. A., Sutherland, R. S., Heisler, C. A., & Trevena, J. 2001, ApJ, 556, 121
Khostovan, A. A., Sobral, D., Mobasher, B., et al. 2015, MNRAS, 452, 3948

Kikuchihara, S., Ouchi, M., Ono, Y., et al. 2020, ApJ, 893, 60
Kojima, T., Ouchi, M., Nakajima, K., et al. 2017, PASJ, 69, 44
Konno, A., Ouchi, M., Nakajima, K., et al. 2016, ApJ, 823, 20
Konno, A., Ouchi, M., Shibuya, T., et al. 2018, PASJ, 70, S16
Kriek, M., Shapley, A. E., Reddy, N. A., et al. 2015, ApJS, 218, 15
Labbé, I., Oesch, P. A., Bouwens, R. J., et al. 2013, ApJL, 777, L19
Lam, D., Bouwens, R. J., Labbé, I., et al. 2019, A&A, 627, A164
Lee, J. C., Ly, C., Spitler, L., et al. 2012, PASP, 124, 782
Li, M., Cai, Z., Bian, F., et al. 2022, arXiv:2211.01382
Ly, C., Malkan, M. A., Kashikawa, N., et al. 2007, ApJ, 657, 738
Madau, P., & Dickinson, M. 2014, ARA&A, 52, 415
Maraston, C., Pforr, J., Henriques, B. M., et al. 2013, MNRAS, 435, 2764
Mármol-Queraltó, E., McLure, R. J., Cullen, F., et al. 2016, MNRAS, 460, 3587
Maseda, M. V., Franx, M., Chevallard, J., & Curtis-Lake, E. 2019, MNRAS, 486, 3290
Maseda, M. V., van der Wel, A., Rix, H.-W., et al. 2018, ApJ, 854, 29
Masters, D., McCarthy, P., Siana, B., et al. 2014, ApJ, 785, 153
Matthee, J., Mackenzie, R., Simcoe, R. A., et al. 2023, ApJ, 950, 67
Matthee, J., Naidu, R. P., Pezzulli, G., et al. 2022, MNRAS, 512, 5960
Matthee, J., Sobral, D., Best, P., et al. 2017, MNRAS, 465, 3637
Naidu, R. P., Matthee, J., Oesch, P. A., et al. 2022, MNRAS, 510, 4582
Naidu, R. P., Tacchella, S., Mason, C. A., et al. 2020, ApJ, 892, 109
Nakajima, K., Ellis, R. S., Iwata, I., et al. 2016, ApJL, 831, L9
Nakajima, K., Ouchi, M., Isobe, Y., et al. 2023, arXiv:2301.12825
Nanayakkara, T., Brinchmann, J., Glazebrook, K., et al. 2020, ApJ, 889, 180
Ning, Y., Cai, Z., Jiang, L., et al. 2023, ApJL, 944, L1
Oke, J. B., & Gunn, J. E. 1983, ApJ, 266, 713
Osterbrock, D. E., & Ferland, G. J. 2006, Astrophysics of Gaseous Nebulae and Active Galactic Nuclei (2nd ed.; Sausalito, CA: Univ. Science Books)
Ouchi, M., Ono, Y., & Shibuya, T. 2020, ARA&A, 58, 617
Pontoppidan, K. M., Barrientes, J., Blome, C., et al. 2022, ApJL, 936, L14
Rasappu, N., Smit, R., Labbé, I., et al. 2016, MNRAS, 461, 3886
Reddy, N. A., Kriek, M., Shapley, A. E., et al. 2015, ApJ, 806, 259
Reddy, N. A., Shapley, A. E., Sanders, R. L., et al. 2018, ApJ, 869, 92
Rhoads, J. E., Wold, I. G. B., Harish, S., et al. 2023, ApJL, 942, L14
Rieke, M. J., Kelly, D. M., Misselt, K., et al. 2023, PASP, 135, 028001
Rigby, J., Perrin, M., McElwain, M., et al. 2023, PASP, 135, 048001
Roberts-Borsani, G. W., Bouwens, R. J., Oesch, P. A., et al. 2016, ApJ, 823, 143
Robertson, B. E. 2022, ARA&A, 60, 121
Sanders, R. L., Shapley, A. E., Jones, T., et al. 2021, ApJ, 914, 19
Sanders, R. L., Shapley, A. E., Topping, M. W., Reddy, N. A., & Brammer, G. B. 2023a, arXiv:2301.06696
Sanders, R. L., Shapley, A. E., Topping, M. W., Reddy, N. A., & Brammer, G. B. 2023b, arXiv:2303.08149
Schaerer, D., & de Barros, S. 2009, A&A, 502, 423
Schaerer, D., Marques-Chaves, R., Barrufet, L., et al. 2022, A&A, 665, L4
Schechter, P. 1976, ApJ, 203, 297
Schlawin, E., Leisenring, J., Misselt, K., et al. 2020, AJ, 160, 231
Schmidt, M. 1968, ApJ, 151, 393
Schouws, S., Stefanon, M., Bouwens, R., et al. 2022, ApJ, 928, 31
Shapley, A. E., Reddy, N. A., Kriek, M., et al. 2015, ApJ, 801, 88
Shen, X., Vogelsberger, M., Nelson, D., et al. 2020, MNRAS, 495, 4747
Shim, H., Chary, R.-R., Dickinson, M., et al. 2011, ApJ, 738, 69
Shivaei, I., Reddy, N. A., Siana, B., et al. 2018, ApJ, 855, 42
Smit, R., Bouwens, R. J., Franx, M., et al. 2015, ApJ, 801, 122
Smit, R., Bouwens, R. J., Labbé, I., et al. 2014, ApJ, 784, 58
Smit, R., Bouwens, R. J., Labbé, I., et al. 2016, ApJ, 833, 254
Sobral, D., Best, P. N., Smail, I., et al. 2014, MNRAS, 437, 3516
Sobral, D., Matthee, J., Best, P., et al. 2017, MNRAS, 466, 1242
Sobral, D., Smail, I., Best, P. N., et al. 2013, MNRAS, 428, 1128
Song, M., Finkelstein, S. L., Ashby, M. L. N., et al. 2016, ApJ, 825, 5
Stark, D. P., Ellis, R. S., Charlot, S., et al. 2017, MNRAS, 464, 469
Stark, D. P., Schenker, M. A., Ellis, R., et al. 2013, ApJ, 763, 129
Stark, D. P., Walth, G., Charlot, S., et al. 2015, MNRAS, 454, 1393
Stefanon, M., Bouwens, R. J., Illingworth, G. D., et al. 2022, ApJ, 935, 94
Stefanon, M., Bouwens, R. J., Labbé, I., et al. 2021, ApJ, 922, 29
Steidel, C. C., Rudie, G. C., Strom, A. L., et al. 2014, ApJ, 795, 165
Steidel, C. C., Strom, A. L., Pettini, M., et al. 2016, ApJ, 826, 159
Strom, A. L., Steidel, C. C., Rudie, G. C., et al. 2017, ApJ, 836, 164
Sun, F., Egami, E., Fujimoto, S., et al. 2022a, ApJ, 932, 77
Sun, F., Egami, E., Pirzkal, N., et al. 2022b, ApJL, 936, L8
Tacchella, S., Bose, S., Conroy, C., Eisenstein, D. J., & Johnson, B. D. 2018, ApJ, 868, 92
Tacchella, S., Johnson, B. D., Robertson, B. E., et al. 2023, MNRAS, 522, 6236
Tadaki, K.-I., Kodama, T., Koyama, Y., et al. 2011, PASJ, 63, 437
Tamura, Y., Mawatari, K., Hashimoto, T., et al. 2019, ApJ, 874, 27
Tang, M., Stark, D. P., Chen, Z., et al. 2023, arXiv:2301.07072
Tang, M., Stark, D. P., Chevallard, J., & Charlot, S. 2019, MNRAS, 489, 2572
Taylor, A. J., Barger, A. J., & Cowie, L. L. 2022, ApJL, 939, L3
Thomas, D., Steele, O., Maraston, C., et al. 2013, MNRAS, 431, 1383
Topping, M. W., Shapley, A. E., Reddy, N. A., et al. 2020a, MNRAS, 495, 4430
Topping, M. W., Shapley, A. E., Reddy, N. A., et al. 2020b, MNRAS, 499, 1652
Torrey, P., Vogelsberger, M., Marinacci, F., et al. 2019, MNRAS, 484, 5587
Trump, J. R., Arrabal Haro, P., Simons, R. C., et al. 2023, ApJ, 945, 35
Trussler, J. A. A., Adams, N. J., Conselice, C. J., et al. 2023, MNRAS, 523, 3423
Wilkins, S. M., Lovell, C. C., Vijayan, A. P., et al. 2023, MNRAS, 522, 4014
Williams, C. C., Curtis-Lake, E., Hainline, K. N., et al. 2018, ApJS, 236, 33
Zavala, J. A., Casey, C. M., Manning, S. M., et al. 2021, ApJ, 909, 165